Opportunistic Rain Rate Estimation from Measurements of Satellite Downlink Attenuation: a Survey

Filippo Giannetti [1,*] and **Ruggero Reggiannini** [1]

[1]   Dipartimento di Ingegneria dell'Informazione, University of Pisa, Pisa 56122, Italy; ruggero.reggiannini@unipi.it

*   Correspondence: filippo.giannetti@unipi.it; Tel.: +39-050-2217-548

Abstract: Recent years have witnessed a growing interest in techniques and systems for rainfall surveillance on regional scale, with increasingly stringent requirements in terms of: *i*) accuracy of rainfall rate measurements, *ii*) adequate density of sensors over the territory, *iii*) space-time continuity and completeness of data, *iv*) capability to elaborate rainfall maps in near real time. The devices deployed to monitor the precipitation fields are traditionally networks of rain gauges distributed throughout the territory, along with weather radars and satellite remote sensors operating in the optical or infrared band, none of which, however, is suitable for full compliance to all of the requirements cited above. More recently, a different approach to rain rate estimation techniques have been proposed and investigated, based on the measurement of the attenuation induced by rain on signals of pre-existing radio networks, either in terrestrial links, e.g. the backhaul connections in cellular networks, or in satellite-to-earth links and, among the latter, notably those between geostationary broadcast satellites and domestic subscriber terminals in the Ku and Ka bands. Knowledge of the above rain-induced attenuation permits to retrieve the corresponding rain intensity provided that a number of meteorological and geometric parameters are known, and ultimately permits to estimate the rain rate locally at the receiver site. In this survey paper we specifically focus on such a type of "opportunistic" systems for rain field monitoring, which appear very promising in view of the wide diffusion over the territory of low-cost domestic terminals for the reception of satellite signals, prospectively allowing for a considerable geographical capillarity in the distribution of sensors, at least in more densely populated areas. The purpose of the paper is to present a broad albeit synthetic overview of the numerous issues inherent in the above rain monitoring approach, along with a number of solutions and algorithms proposed in the literature in recent years, and ultimately to provide an exhaustive account of the current state of the art. Initially, the main relevant aspects of the satellite link are reviewed, including those related to satellite dynamics, frequency bands, signal formats, propagation channel and radio link geometry, all of which have a role in rainfall rate estimation algorithms. We discuss the impact of all these factors on rain estimation accuracy, also highlighting the substantial differences inherent in this approach in comparison with traditional rain monitoring techniques. We also review the basic formulas relating rain rate intensity to a variation of the received signal level or of the signal-to-noise ratio. Furthermore, we present a comprehensive literature survey of the main research issues for the aforementioned scenario and provide a brief outline of the algorithms proposed for their solution, highlighting their points of strength and weakness. The paper includes an extensive list of bibliographic references from which the material presented herein was taken.

1. Introduction

Real-time monitoring of atmospheric precipitations over a regional territory is an objective of primary importance for public administrators to be pursued in the context of prevention policies aimed at ensuring an adequate level of safety for people living or working in the area ([1]-[6], just to cite a few). In the above perspective, it is of interest to have updated rainfall maps constantly available, featuring *i*) good accuracy in rainfall rate (RR) measurements, *ii*) space-time completeness and continuity, and *iii*) negligible delays in rain data provisioning, so as to allow timely prediction of the rainfall distribution for any incumbent meteorological event and, when required, early adoption of adequate countermeasures to prevent or reduce the related risk.

The tools traditionally available for the estimation/prediction of rain maps belong to three categories, namely *i*) a set of rain gauges distributed throughout the territory and connected to a real-time data collection network, *ii*) a network of meteorological radars, *iii*) deployment of weather satellites (typically geostationary, such as Meteosat satellites) for remote sensing of cloud formations and whether perturbations. However, each of these methods taken individually is not able to fully satisfy the aforementioned requirements, and their joint use for a really pervasive coverage of an entire vast region would entail formidable costs for the provisioning and deployment of (notably radar) sensors and for the infrastructure required for their integration and coordination [6]-[8].

More recently, additional "opportunistic" methods have been proposed for estimating the RR, which exploit the existence of radio links distributed throughout the area, even if installed for other purposes. Basically these systems are of two types: *i*) service or ancillary terrestrial radio links, e.g. for cellular mobile networks (specifically, backhaul links

49 from the radio access nodes to infrastructure [9], [10], [11]) or those used in other fixed terrestrial networks [2], [12] and
50 ii) radio links operating between satellites and fixed terrestrial terminals distributed throughout the territory, notably
51 for satellite-to-home TV broadcast services provided to domestic subscribers (e.g. [1], [3], [4], [6], [13], [14]).

52 The idea behind all these techniques is to measure the global attenuation introduced by the rain on the received signal,
53 which is an integral function of the rainfall distribution along the radio path [15], and subsequently attempt to trace the
54 value of RR producing this attenuation at all points of the link by means of specific inversion algorithms.

55 In the case of terrestrial radio links, this usually leads to the use of tomographic techniques that allow to estimate the
56 rain field at a generic geographical site starting from attenuation measurements collected from different radio links that
57 intersect one another in the vicinity of the site [16]. The resulting estimation accuracy depends on number, density and
58 variety of directions of the available radio paths.

59 On the other hand, in the case of a satellite link, where the radio path segment affected by the rain is very short and
60 adjacent to the terrestrial terminal, it is often possible to achieve a relatively accurate estimate of the RR in proximity to
61 the terrestrial receiver with a very simple inversion algorithm directly mapping the measured attenuation onto the RR
62 estimate. These latter techniques are of particular interest since they allow to carry out as many measurements of RR
63 over the territory as there are usable terminals and therefore, in the presence of a large population of resident subscrib-
64 ers, they could prospectively offer a vast and capillary coverage of the region. For this reason they have been the subject
65 of considerable attention in the last couple of decades, and although initially they might have been viewed as support
66 systems or gap fillers for preexisting rain monitoring infrastructures, later on they have been considered as a viable
67 low-cost stand-alone measurement alternative.

68 With reference only to systems using satellites for RR estimation, which is the focus of this paper, a host of solutions
69 have been proposed and analyzed that differ from each other based on the criteria used to define the numerous subsys-
70 tems and parameters involved in the estimation procedure. The first to be considered here is the type of opportunistic
71 target satellite which obviously impacts the receiving antenna design and may require additional hardware to track the
72 satellite position. Currently, the most mature technology in the field of opportunistic RR estimation from satellite signals
73 relies on geostationary orbit (GEO) satellites (i.e., placed on a circular orbit laying on the equatorial plane, approximately
74 at 35,800 km above the Earth surface). Recently, the use of Low-Earth Orbit (LEO) satellites (i.e., moving on variously-
75 inclined circular orbits at 160 – 2,000 km above the Earth surface, typically arranged in constellations) was proposed as
76 well [17], [18]. Among the various other aspects to be carefully considered in the RR estimator design, we mention i)
77 choice of the operating frequency, impacting the sensitivity of the receiver to rain; ii) choice of the rain-sensitive param-
78 eter, i.e., subject to a variation in the presence of rain, to be extracted from the received waveform (either the received
79 signal power or the signal-to-noise ratio); iii) selection and cost evaluation of the receiving hardware, either available
80 commercially off-the-shelf or requiring a dedicated implementation; iv) development of the processing algorithm to be
81 applied to measurements; v) retrieval of auxiliary information relating to the radio link geometry; vi) retrieval of climatic
82 and meteorological data involved in the RR estimation algorithm; vii) methods to build rain maps etc.

83 In this paper we attempt to sort and classify the huge amount of material available in the literature on the above topics.
84 We present, on the one side, a comprehensive overview of the main inherent issues to be dealt with and, on the other
85 side, we review and discuss the techniques proposed for their solution, highlighting their points of strength and weak-
86 ness.

87 The paper is organized as follows. Initially (Section 2) the basic concepts of satellite radio communications are reviewed,
88 with particular reference to geostationary satellites, by far the most commonly used for opportunistic RR measurements,
89 and the link budget equations are recalled for the frequency ranges used in the downlink. In Section 3 we review the
90 various impairment factors that can reduce the received signal level in addition to the free-space loss, initially (Section
91 3.1) in the absence of precipitations, with regard to the phenomena occurring in the propagation through the ionosphere
92 and troposphere, and also considering the effect of station keeping maneuvers and pointing errors of the terrestrial
93 antenna. Next (Section 3.2) we discuss some models used to predict the attenuation introduced by stratiform rain both
94 in the melting layer and in the liquid layer, highlighting how the specific attenuation affecting the signal is related to
95 the RR. In Section 4 we review the techniques used to measure the attenuation introduced by rain on the received signal
96 and the elaborations needed to estimate the RR. Specifically, two widely used techniques are compared and discussed,
97 the first based on the measurement of the satellite beacon level, the other on the evaluation of the signal-to-noise ratio
98 of a digital payload signal. Furthermore, the analytical tools to obtain the RR estimate from the measured attenuation
99 are reviewed, also discussing the impact of the precipitation model and the possible non-uniformity of rain on the radio
100 path. The substantial differences inherent in this approach in comparison with traditional rain monitoring techniques
101 are also addressed. Subsequently, in Section 5 we provide an extensive survey of the techniques proposed in the litera-
102 ture for the estimation of the RR, based on measurements of attenuation of a satellite signal. The presentation is orga-
103 nized by sequentially addressing each of the issues inherent in this application, as pointed out above, and by briefly

104 illustrating how the various authors deal with them and propose tailored solutions. Finally Section 6 concludes the
105 paper. An extensive list of bibliographic references is included from which the material presented herein was taken.

2. Review of satellite radio links

107 In this paper we consider the monitoring and utilization of the downlink signals from telecommunication satellites to
108 fixed terrestrial receiving stations, also termed herein ground stations (GSs). The goal is the opportunistic estimation of
109 the RR via signal attenuation measurements. Since rain attenuation significantly affects microwave satellite communi-
110 cation at frequencies above 10 GHz, we will focus our attention on satellite services in the Ku band and above. These
111 bands are assigned to direct-to-home (DTH) television (TV) broadcast from GEO satellites, and also to two-way broad-
112 band services, either with GEO or LEO satellites. The frequency bands allocated to these services, with reference to ITU
113 Region 1, are illustrated in Table 1.

114   **Table 1.** Frequency bands for the downlink of communication satellites, above 10 GHz (ITU Region 1).

Band	Frequency (GHz)	Service	Direction	Ref.
Ku	10.70 – 12.75	Space-to-Earth, Fixed-Satellite Broadcasting-satellite service	downlink	[19]
Ka	17.30 – 20.20	Space-to-Earth, Fixed-Satellite Broadband satellite service	downlink	[20]
Ka	21.40 – 22.00	Space-to-Earth, Fixed-Satellite Broadcasting-satellite service	downlink	[21]
Q/V	37.50 – 43.50	Space-to-Earth, Fixed-Satellite: Broadband satellite service	downlink	[22]

2.1. A simple geometrical model of the satellite link through the troposphere

117 The downlink from a satellite to a GS in the presence of rain is shown in schematic form in Figure 1, where we assume
118 stratiform precipitation. For now, we also assume a clear separation between two layers (tropospheric models with
119 more layers will be addressed later). The upper layer, named "ice particles layer" (IPL), is mostly made of ice in the form
120 of frozen dry particles, which exhibit very low scattering cross sections. This region is therefore associated with very
121 small specific attenuations [23] and in the following its contribution to the attenuation of the satellite signal will be
122 neglected. The lower layer, named "liquid layer" (LL), is instead characterized by the presence of the liquid-phase pre-
123 cipitation originated by ice particles that are completely melt into raindrops, and introduces significant excess attenua-
124 tion on the satellite signal. In such a simplified model, the boundary between the two layers, where the rain originates,
125 has height h_R and is assumed coincident with the height of the 0 ℃ isotherm, denoted as h_0.
126 The GS is located at an altitude h_S above mean sea level (MSL) and sees the satellite at an elevation angle θ above the
127 horizon. The final part of the slanted electromagnetic path crosses then the LL along a segment of length L_S, named
128 the "wet segment". For a given setting of the link parameters, the rain introduces an attenuation in an extent that de-
129 pends on L_S and on the distribution of the rain field along the wet segment. If the satellite is of the GEO type, it is seen
130 by the terrestrial receiver under fixed azimuth/elevation (AzEl) angles, and the wet path segment also has a fixed direc-
131 tion with respect to a terrestrial reference. Therefore, the measurement of the rain attenuation experienced by the re-
132 ceived signal provides an integral metric of the rain field along the wet segment. Under the assumption that the rain
133 field is approximately constant along the wet segment (as supposed in many of the works available in the literature on
134 the subject), the local value of the rain rate (RR) at the receiver location can be obtained from the measurement of the
135 attenuation, regardless of the satellite position, provided that the length of the wet segment and the mapping law be-
136 tween specific attenuation and RR are known (see Section 3.2 for details). If the assumption about the constant value of
137 the rain field on the wet segment does not hold, measuring the attenuation affecting the downlink signal from a GEO
138 satellite does no longer allow to achieve a fully reliable estimate for the point-scale value of RR. In this case, an alterna-
139 tive approach commonly pursued in the literature consists in measuring (either simultaneously or sequentially) the
140 attenuation undergone by different signals arriving from several satellites that are in visibility on the geostationary arc
141 at different AzEl angles. By this way, the corresponding wet segments intersect the rain field along a wide variety of
142 directions, and therefore tomographic techniques could be proficiently applied to estimate the rain field. Table 2 enu-
143 merates all of the GEO satellites for DTH TV broadcasting in the Ku band that have at least one beam covering the city
144 of Pisa, Italy (10.4147° E, 43.7117° N), while Figure 2 shows their positions on the orbital arc. For each satellite, Table 2
145 specifies the orbital longitude, along with the AzEl coordinates and the EIRP (effective isotropic radiated power) for a
146 GS located in Pisa. This example demonstrates that many GEO satellites are potentially available for rain monitoring
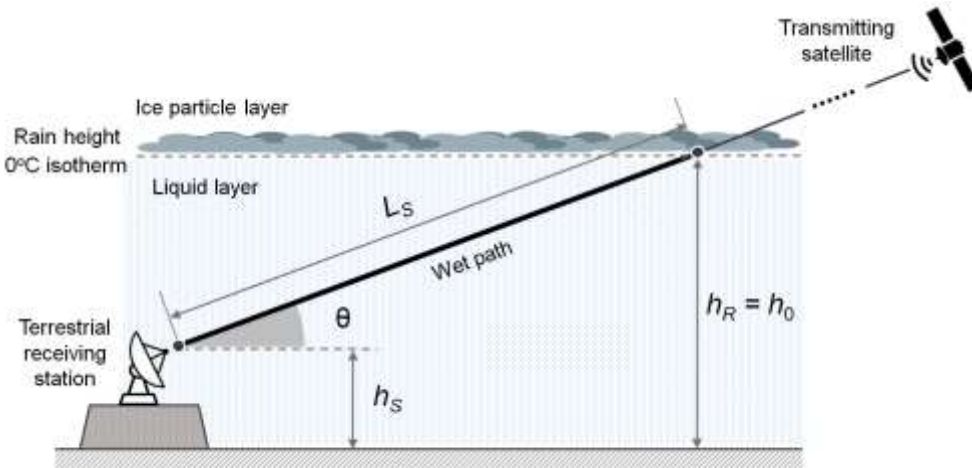147 from a single receive site.

148

149

150   **Figure 1.** Satellite downlink geometry in the presence of stratiform rain and two-layer tropospheric model.
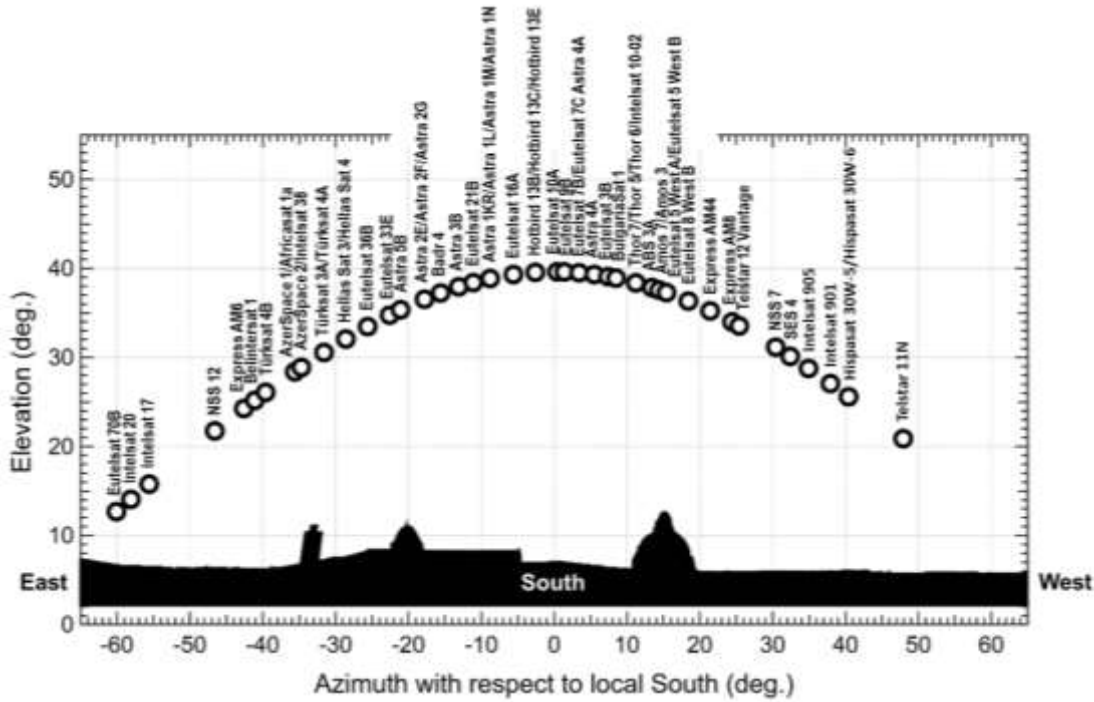
151

152

153   **Figure 2**. Geostationary satellite arc in the sky of Pisa, Italy (10.4147° E, 43.7117° N).

154 **Table 2.** List of geostationary satellites for DTH TV broadcasting in the Ku band
155 that can be received in Pisa, Italy (10.4147° E, 43.7117° N).

Geostationary Satellite	Long. (deg.)	Azimuth w.r.t. local South (deg.)	Elevation above horizon (deg.)	Beam	EIRP (dBW)	Reference
Eutelsat 70B	70.5	-60.0853	12.6724	Wide	44	www.lyngsat.com
Intelsat 20	68.5	-58.0853	14.0569	Europe & Africa	44.8	www.lyngsat.com
Intelsat 17	66.0	-55.5853	15.7709	Europe & Mid-East	47.6	www.digisat.org
NSS 12	57.0	-46.5853	21.7379	Middle East	46	www.lyngsat.com
Express AM6	53.0	-42.5853	24.2543	Fixed 2	47	www.lyngsat.com
Belintersat 1	51.5	-41.0853	25.1708	Europe	51	belintersat.com
Türksat 4B	50.0	-39.5853	26.0710	West	54	satstar.net
AzerSpace 1/Africasat 1a	46.0	-35.5853	28.3825	Europe	46	satstar.net
AzerSpace 2/Intelsat 38	45.1	-34.6853	28.8831	Europe	51.6	www.lyngsat.com
Türksat 3A/Türksat 4A	42.0	-31.5853	30.5469	West	52	www.lyngsat.com
Hellas Sat 3/Hellas Sat 4	39.0	-28.5853	32.0591	Europe FSS	52	satstar.net
Eutelsat 36B	36.0	-25.5853	33.4642	Eurasia	48	www.lyngsat.com
Eutelsat 33E	33.0	-22.5853	34.7513	Wide	50	satstar.net
Astra 5B	31.5	-21.0853	35.3471	High power	52	www.lyngsat.com
Astra 2E/Astra 2F/Astra 2G	28.2	-17.7853	36.5375	Europe	50	www.lyngsat.com
Badr 4	26.0	-15.5853	37.2336	BSS	47	www.arabsat.com
Astra 3B	23.5	-13.0853	37.9242	Europe	51	www.lyngsat.com
Eutelsat 21B	21.5	-11.0853	38.3962	Western	46	www.lyngsat.com
Astra 1KR/Astra 1L/Astra 1M/Astra 1N	19.2	-8.7853	38.8473	Europe	51	www.lyngsat.com
Eutelsat 16A	16.0	-5.5853	39.3062	Europe B	50	www.lyngsat.com
Hotbird 13B/Hotbird 13C/Hotbird 13E	13.0	-2.5853	39.5528	Wide	53	www.lyngsat.com
Eutelsat 10A	10.0	0.4147	39.6185	Wide	48	www.lyngsat.com
Eutelsat 9B	9.0	1.4147	39.6000	Wide	51	www.lyngsat.com
Eutelsat 7B/Eutelsat 7C	7.0	3.4147	39.5026	Europe A	49	www.eutelsat.com
Astra 4A	4.9	5.5147	39.3140	Europe BSS	50	www.lyngsat.com
Eutelsat 3B	3.0	7.4147	39.0683	Europe	49	www.lyngsat.com
BulgariaSat 1	1.9	8.5147	38.8938	Europe	50	www.lyngsat.com
Thor 7/Thor 5/Thor 6/Intelsat 10-02	-0.8	11.2147	38.3679	Spot 1	53.2	www.lyngsat.com
ABS 3A	-3.0	13.4147	37.8395	Europe	50	absatellite.com
Amos 7/Amos 3	-4.0	14.4147	37.5706	Pan European	53	www.amos-spacecom.com
Eutelsat 5 West A/Eutelsat 5 West B	-5.0	15.4147	37.2842	Super	53	www.lyngsat.com
Eutelsat 8 West B	-8.0	18.4147	36.3237	Europe	54	satstar.net
Express AM44	-11.0	21.4147	35.2191	S1	51	www.lyngsat.com
Express AM8	-14.0	24.4147	33.9811	Fixed 1	51	www.lyngsat.com
Telstar 12 Vantage	-15.0	25.4147	33.5407	Europe & Middle East	51	satstar.net
NSS 7	-20.0	30.4147	31.1490	Europe & Middle East	49	satstar.net
SES 4	-22.0	32.4147	30.1113	Europe & Middle East	49	www.lyngsat.com
Intelsat 905	-24.5	34.9147	28.7563	Spot 1	52.6	www.lyngsat.com
Intelsat 901	-27.5	37.9147	27.0528	Spot 2	45	satstar.net
Hispasat 30W-5/Hispasat 30W-6	-30.0	40.4147	25.5753	Europe	54	www.lyngsat.com
Telstar 11N	-37.5	47.9147	20.8807	Europe	52	satstar.net

156

157 *2.2. Satellite link budget*

158 We now briefly review the link budget for the downlink of a GEO satellite. For the moment, we assume the EIRP seen
159 at the receiver site takes on the nominal value provided by the satellite operator, thus neglecting any fluctuation of the
160 received power due to residual orbit inclination w.r.t. the equatorial plane, as well as to antenna pointing errors and to
161 propagation impairments (these issues will be addressed in Section 3). Then the available power of the useful signal
162 (also termed "carrier") at the receiver is expressed by

163
$$C = \frac{\text{EIRP}}{L_{\text{FS}} L_{\text{atm}} L_{\text{rain}}} G_{\text{R}} \tag{1}$$

164 Where L_{FS} is the free-space loss, L_{atm} is the atmospheric attenuation due to gaseous absorption (in the absence of rain),
165 L_{rain} is the additional attenuation due to rain, which is the target parameter to track in order to achieve rain estimation,
166 and G_{R} is the gain of the receiving antenna of the GS. Also, for a digital signal with bit rate R_b, modulation alphabet
167 size M and coding rate r (i.e, mod/cod (M , r)), the average received energy per bit and per symbol at RF is ex-
168 pressed by $E_b = C/R_b$ and $E_s = C/R_s$, respectively, where $R_s = R_b/(r \log_2 M)$ is the symbol rate. Moreover, for both
169 the "no rain" and "rain" conditions, the available power N of the additive white Gaussian noise (AWGN), at the receiver,
170 within a given bandwidth B (not specified here) can be expressed as

171
$$N = N_0 B \tag{2}$$

172 where $N_0 = k_{\text{B}} T_{\text{eq}}$ is the one-sided noise power spectral density, k_{B} being the Boltzmann constant and T_{eq} the equiv-
173 alent noise temperature of the whole receiving system, given by

174
$$T_{\text{eq}} = T_{\text{A}} + T_{\text{RX}}, \tag{3}$$

175 In (3), T_{RX} is the noise temperature of the receiver (assumed fixed) while T_{A} is the equivalent noise temperature of the
176 antenna, given by

177
$$T_{\text{A}} = \frac{T_c}{L_{\text{atm}} L_{\text{rain}}} + T_{\text{atm}} \left(1 - \frac{1}{L_{\text{rain}} L_{\text{atm}}} \right) + T_g, \tag{4}$$

178 where T_c is the noise temperature of the cosmic background microwave radiation (CBMR), T_{atm} is the mean thermo-
179 dynamic temperature of troposphere and rain (assumed to be equal) and T_g is the elevation-dependent noise spillover
180 temperature, accounting for the noise originated from the surrounding environment, mainly from the ground, and
181 picked-up by the secondary lobes of the receiving antenna. For the sake of exemplification, Table 3 shows the values of
182 the main downlink parameters of a DTH TV broadcast service in the Ku band and DVB-S2 format [24], with a commer-
183 cial-quality receiver [8].
184 The quality of the received signal is expressed by the so-called signal-to-noise ratio (SNR), i.e., the ratio between the
185 power C of the useful signal (see (1)) and the power of the channel noise N (see (2)) collected over a given bandwidth B,
186 with both the powers evaluated at the output of the receiving antenna. This ratio is thus expressed as C/N and applies
187 to any type of "carrier" signal, either analog or digital, either modulated or unmodulated, in the latter case also termed
188 "continuous wave" (CW). In the common case of a digitally-modulated carrier, the signal quality is more conveniently
189 expressed by the ratio between the average energy per symbol E_s received at RF and the noise power spectral density
190 N_0, named energy-per-symbol-to-noise density ratio (ESNDR) and denoted as E_s/N_0.

191 **Table 3**. Parameters of a DTH TV broadcast satellite downlink [8]. LVP: linear vertical polarization. QPSK: quadrature phase shift
192 keying. DVB-S2: digital video broadcasting via satellite, 2nd generation. FEC: forward error correction. QEF: quasi error free, refers
193 to PER =10^{-7} (see [20], Tab. 13). PER: packet error rate.

Receiving location	Pisa, Italy (10.4147° E, 43.7117° N)
Satellite name, orbital slot, inclination	Eutelsat 10A, 10° East, 0.072 °
Satellite EIRP	48 dBW
Frequency, polarization	11.345 GHz, LVP
Protocol, modulation, FEC rate	DVB-S2, QPSK, 4/5
Required ESNDR for QEF performance	4.68 dB
Figure of noise of the receiver	0.2 dB @ 290 K
Noise temperature of the receiver, T_{RX}	13.7 K

Atmospheric attenuation, L_{atm}	0.09 dB
Mean thermodynamic temperature of troposphere, T_{atm}	275 K
Noise temperature of the CBMR, T_c	2.78 K
Noise spillover temperature, T_g	10 K
Receiving antenna diameter, gain (60% efficiency)	80 cm, 37.34 dBi
Typical received ESNDR in clear-sky conditions E_s/N_0	10.5 dB
Link margin	5.82 dB
θ	40°

194

3. Satellite downlink impairments

We hereby briefly review the main factors affecting the received signal level from a GEO satellite downlink. As examples, we refer to the measurements plotted in Fig. 3, relevant to a 6-week record of the ESNDR received from the satellite link described in Table 3.

3.1. Attenuation factors affecting signal level without rain (in addition to free space loss)

3.1.1. Effect of ionosphere and troposphere

In the transit through the ionosphere and troposphere, the downlink signal is subject to scintillation fading [25], with rapid amplitude fluctuations caused by small-scale irregularities in the medium refractive index. This effect is significant for frequencies above 10 GHz and grows with frequency. In Ku band, fluctuations are within ±0.5 dB and the period of scintillation fades varies from 1 to 10 s. Accordingly, the spectral width of these fluctuations in the Ku band is in the order or less than 1 Hz [25]. These fluctuations are much faster than the rain events and even faster if compared to the long-term effects mentioned below (Section 3.1.2). Besides free-space propagation loss, other attenuation factors affecting the satellite downlink are related to the presence of clouds and atmospheric absorption. The latter mainly depends on the environmental conditions (air pressure, temperature and humidity) in the vicinity of the receiving antenna, as well as on the geometry of the connection (altitude h_s of the receiver above MSL and angle of elevation θ of the antenna) and on the operating frequency [26]. For the Ku band, it typically assumes a value of the order of a fraction of dB, with very slow variations over time, induced by the evolution of environmental conditions. Slightly larger values can be found at higher frequencies. Furthermore, the presence of clouds can affect the received signal level [27], reducing it by fractions of a dB, with slow variability over time. Finally, large-scale changes in the medium refractive index due to temperature and humidity gradients may induce downlink path bending [28]. In consequence, the received signal power may experience very slow variations. This effect however is significant only at very low antenna elevation angles (say around 10° or less).

3.1.2. Antenna mispointing and orbit perturbations

Over time, the GEO satellite is subject to many perturbing forces that make it impossible to maintain its orbit perfectly stable and cause a drift both in longitude and latitude. One of the main orbit perturbations is related to the gravitational effects of the moon and the sun that cause a progression of the orbit inclination [29]. The residual orbit inclination and eccentricity cause an apparent daily movement of the satellite in elevation and longitude, as seen from the ground station, along an 8-shaped path, with a 24 hours period [30]. Further variations of the received signal level are caused by the slow longitudinal drift of the satellite orbital position. This is due to gravitational forces caused by earth longitudinal mass variations (for instance, satellites with longitudes from 0° to 60° East, slowly drift eastwards toward the Indian Ocean), and this sums up to the effect of orbit inclination. These perturbations are periodically counteracted by the satellite operator via orbit correction maneuvers, termed "station-keeping": "east–west" and "north–south" station-keeping maneuvers compensate for longitudinal and latitudinal variations, respectively [31]. So, even if the GS antenna is correctly pointing towards the satellite nominal position, its actual gain in the link budget undergoes continuous fluctuations caused by the satellite movements, thus producing the nearly-periodic daily variations of signal strength visible in Figure 3, along with a slow decay associated to the longitudinal drift. All of the above are, however, long-term effects and their evolution is far slower than the signal fluctuations occasionally induced by a rain shower.

3.1.3. Sun blinding

Twice a year, the GS antenna pointing at a GEO satellite is occasionally "blinded" by the apparent passage of the sun behind the satellite. This phenomenon, known as "sun transit", lasts a few minutes every day at the same time over a period of a few days. An example is shown in Figure 3, recorded around the autumn equinox in Pisa, Italy. During the sun transit the antenna noise temperature increases abruptly and may lead to severe deterioration of the SNR. However,

237 the day/time coordinates and persistence of any sun transit can be exactly predicted, and the resulting sun-induced
238 outage (i.e., out-of-service) events can be easily recognized and counteracted in the RR estimation procedure.

239 3.1.4. Operator-induced power variations

240 Occasionally, the satellite operator corrects the satellite orbital position and attitude, or changes the transponder gain
241 setting due to customer requests or other operational needs. The above adjustment is normally carried out in a very
242 short time, and sometimes it involves a reduction in the received power. When any such event occurs, any algorithm
243 used to process the received data may misinterpret it as the onset of a precipitative event unless proper countermeasures
244 are taken (Section 4.5.2). A couple of such events have been observed during the measurements shown in Figure 3.

245 *3.2. Extra attenuation due to rain*

246 Figure 1 schematically shows the radio downlink between a satellite and the GS, in the presence of stratiform rain,
247 assuming a simplified two-layer tropospheric model, made of IPL and LL. As already pointed out, the rain in the LL
248 affecting the final segment of the electromagnetic path may introduce an additional non-negligible attenuation on the
249 received signal if the downlink frequency is close to or above 10 GHz [15] (ch. 9), while the impact of IPL is negligible.
250 While most papers adopt the simple stratification scheme of Figure 1, some authors have investigated the more accurate
251 three-layer tropospheric model depicted in Figure 4. Here, the lower layer containing the GS is the usual liquid layer
252 (LL), above which there is an intermediate layer, called melting layer (ML), where the ice particles falling from the
253 clouds gradually melt [32]-[34]. The upper edge of the ML is the freezing level (i.e., the 0 ºC isotherm) while its lower
254 edge is the level of complete liquefaction of ice, denoted as ML-LL interface in Figure 4 and located a few hundred
255 meters below the 0 °C isotherm. The "wet segment" along the slanted path is now made of two parts: one in the LL, of
256 length L_{LL}, and the other one in the ML, of length L_{ML}.
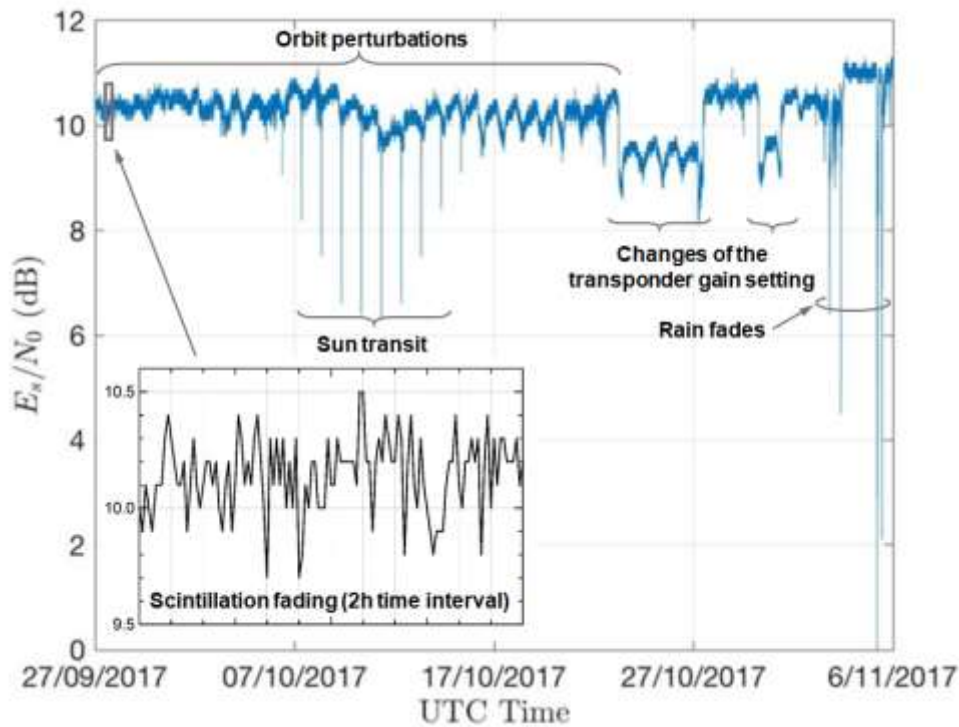257

258

259 **Figure 3**. Record of received E_s/N_0 from the GEO satellite downlink described in Table 3, over a 6-week interval.
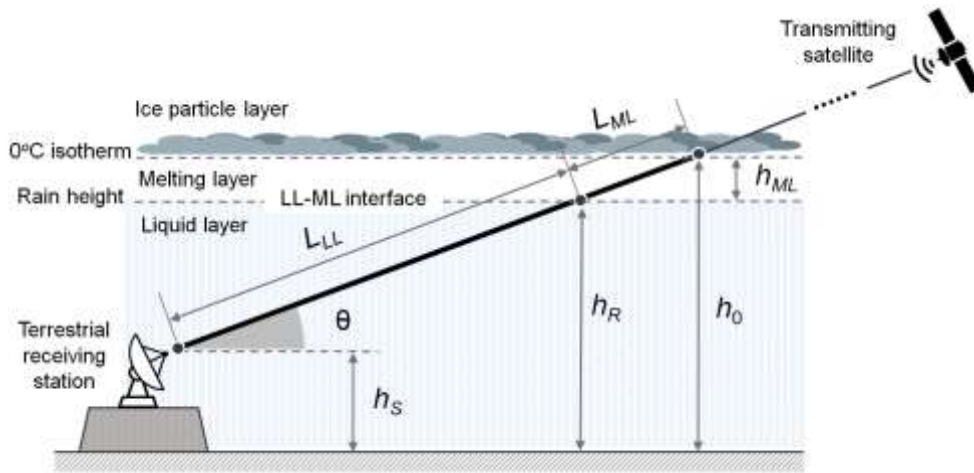
Figure 4. Satellite downlink geometry in the presence of stratiform rain and three-layer tropospheric model.

Taking into account the new layering model, the attenuation induced on the satellite signal by the precipitation is to be ascribed to both the liquid and melting layers, while the contribution of upper layers, above the freezing point, can be neglected. A simplifying assumption that is often formulated when dealing with stratiform rain models, is that the parameters characterizing the rain field are independent of the horizontal coordinates, which implies in particular that the RR is uniform on all points of the slanted electromagnetic path through the LL. This conjecture may not always be so accurate for rain cells having size comparable or smaller than the length of the wet segment, or during the initial and final phases of transit of a weather perturbation front over the receiver site.

3.2.1. Specific attenuation model for the LL

In LL, the signal attenuation is characterized by the specific *logarithmic* attenuation k (in dB/km), which is empirically related to the RR (mm/h) by a weak exponential relationship, also termed "power-law", such as [35]

$$k = aR^b \text{ , dB/km,} \tag{5}$$

where the coefficients a and b depend mainly on carrier frequency, as well as on other climatic, geometric and electromagnetic parameters of the connection, such as temperature, inclination of the rain with respect to the electromagnetic path and polarization. While a varies by orders of magnitude with the frequency in the range from 1 GHz to a few tens of GHz, b varies much less and does not differ very much from unity. Model (5) is assumed to be valid by all authors, even if the choice of the coefficients a and b is somewhat not uniform from author to author. Several authors (e.g. [1], [6]) refer to the values of a and b recommended in [36], while others use values taken from the literature (as in [15], [26]), or derived from *ad hoc* experiments carried out in geographical areas of specific interest [3], [37], [38].

3.2.2. Specific attenuation model for the ML

With reference to a stratiform precipitation and to the model in Figure 4, the ML is defined as that layer characterized by the coexistence of solid phase (ice) and liquid phase (rain). It can be argued that the effect of the ML on signal attenuation depends both on how the liquid fraction of the precipitation varies as a function of the vertical coordinate, and on the law the liquid fraction maps onto a specific attenuation value. Since there are no consolidated results/models to describe the above phenomena, various approximate approaches have been followed in the literature. One of them is to assume fictitiously that the ML is made entirely of liquid phase like the LL, so that model (5) holds for the ML as well, but with a different choice for the parameters a and b [32]-[34], [39]. According to this scheme, the overall attenuation is calculated as that resulting from the series of two attenuators (ML and LL) undergoing the same RR as the LL. A variant to this scheme is to retain the simplified model in Figure 1 and fictitiously modify (increase) the LL height to take into account the impact of the ML [26], [36], while keeping the same values for a and b valid for the LL. Further analytical *ad hoc* models have been developed by other authors, e.g. in [8], [40]. Additional details on these topics are given in Section 5.4.2.

4. Basic methods for estimating the rainfall rate from rain attenuation

In the following, the absence of rain, i.e., the case $L_{rain} = 1$ (0 dB), will be referred to as the "clear-sky" condition and the parameters relevant to this condition will be therefore denoted by the subscript "clear".

4.1. Basic methods for measuring rain attenuation

297 We now outline two basic schemes proposed in the literature for evaluating the attenuation incurred by the satellite
298 signal in the downlink. The first one is based on the exploitation of the beacon signal transmitted by the satellite, while
299 the other relies on the direct elaboration of the DVB-S/S2 signal broadcast by the satellite transponder.

300 4.1.1. Beacon power measurement

301 Beacons are narrow-band signals transmitted by the satellites, most often in horizontal (H) polarization, which are either
302 unmodulated (also termed "continuous wave", or CW) and mainly intended for antenna steering and power control-
303 purposes, or digitally-modulated by FSK or PSK and carrying low-rate (i.e., a few kbit/s) telemetry (TM) data [41].
304 Beacons allow the operator to monitor satellite status and position, but they can also be used by customers for antenna
305 tracking. In the case of broadcast satellites, typical values for the EIRP are 9 dBW for CW [42], [43] and 4 dBW in case
306 of TM [43]. Figure 5 (from [44]) illustrates a simplified version of the frequency plan of the Ku band geostationary
307 satellite Eutelsat 10A, located at 10° E. The arrows represent the beacons, that are allocated at the sides of the frequency
308 spectrum occupied by the transponders [45]: double-arrow symbols indicate TM beacons with binary FSK modulation,
309 while single arrows indicate CW beacons.

310 Instead the beacons radiated by communication satellites providing two-way broadband services in the Ka band to both
311 fixed and mobile users with multiple-spot-coverage, have stronger levels (typically, 30 dBW [46]). In this case, a beacon
312 is radiated inside each beam and is used by the service customer for initial pointing of the antenna, for satellite tracking
313 (in case of mobile reception), and for enabling uplink transmissions and power control.

314 Due to their constant transmit power, beacons represent an excellent reference for the measurement of the fluctuations
315 in received signal strength caused by propagation phenomena. Figure 6 depicts the high-level conceptual scheme of the
316 beacon-based measurement system, which was adopted by many authors [6], [47]-[51].
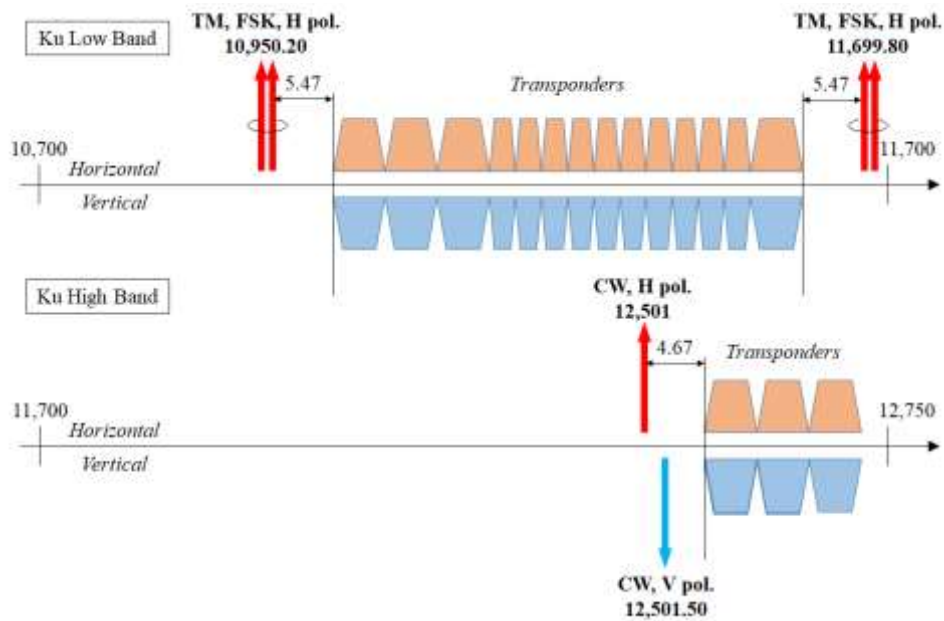
317

318

319 **Figure 5**. Simplified frequency plan (not to scale) of the Ku band geostationary satellite Eutelsat 10A, located at 10° East [44], show-
320 ing polarization and frequency allocation of the beacons [45]. All the frequencies are in MHz. A single arrow indicates a CW beacon,
321 while a double-arrow symbol represents a binary FSK-modulated TM beacon.
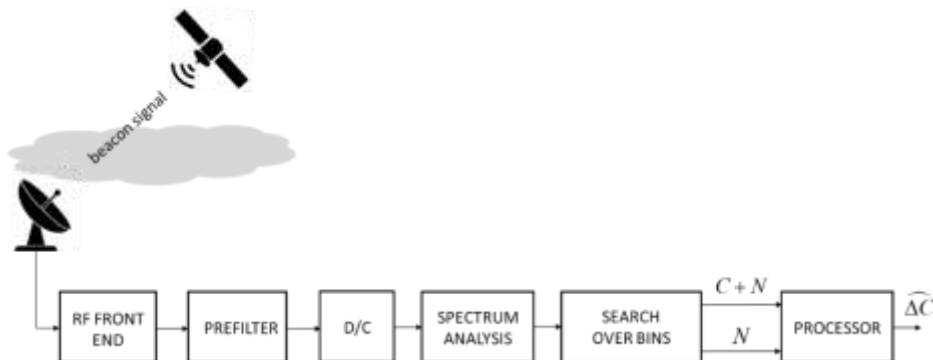

322

323 **Figure 6**. High-level block diagram of a beacon receiver for the estimate of the carrier attenuation.

After the RF front-end, a CW beacon is prefiltered by a narrowband band-pass filter centered around the beacon frequency. The passband is, however, wide enough (it can be in the order of magnitude of one hundred kHz) to accommodate the frequency instability of the beacon generator which is typically in the order of 1 ppm per annum, and also the transmitter phase noise, whose band is just a few tens of Hz. The prefilter is followed by a down-conversion to baseband (the block "D/C" in Figure 6). Then, a vernier search in frequency of the beacon signal is carried out by means of a filter bank made, for example, with an FFT-based spectrum analyzer (the "Spectrum Analysis" block in Figure 6). The analyzer resolution is a few tens of Hz, and in any case not narrower than the band broadening induced by the overall phase noise of both the transmitter and the receiver. The analysis bin corresponding to the maximum level provides then a measure of the sum of the beacon power C and that of the noise N within the resolution band (i.e., the bin width), while the farthest bins (at the edges of the band) give a measure of the noise N only.

From these measurements, made during both rain and clear-sky conditions, it is therefore possible to evaluate the reduction of the beacon power ΔC, representing an estimate of the rain attenuation L_{rain}. In this respect, it is worth remarking that the presence of rain (i.e., $L_{\mathrm{rain}} > 1$) has a twofold effect: on the one side, it reduces the power of the useful signal (the beacon, in this case), as in (1) while on the other side it increases the noise power, as can be inferred from (2)-(4). Therefore it is not correct to ascribe the SNR degradation to the variation of C alone, although some authors seem to ignore or overlook this issue.

Recalling (1)-(4), it is possible to derive a formula for estimating the rain attenuation L_{rain} from measurements of the received power, both in the absence and presence of rain. The total received power within the frequency bin containing the beacon carrier (for the sake of simplicity, we assume hereafter that there is no power leakage on adjacent bins) can be expressed as follows

$$P_{\mathrm{rain}}\left(L_{\mathrm{rain}}\right) = C + N = \frac{\mathrm{EIRP}}{L_{\mathrm{FS}}L_{\mathrm{atm}}L_{\mathrm{rain}}}G_{\mathrm{R}} + k_{\mathrm{B}}B\left[\frac{T_c}{L_{\mathrm{atm}}L_{\mathrm{rain}}} + T_{\mathrm{atm}}\left(1 - \frac{1}{L_{\mathrm{atm}}L_{\mathrm{rain}}}\right) + T_g + T_{\mathrm{RX}}\right]. \quad (6)$$

where B denotes here the analyzer frequency resolution (i.e., the bin width); also, the dependence of the received power P_{rain} on the rain attenuation L_{rain}, has been pointed out. Now, let us denote with $P_{\mathrm{clear}} = P_{\mathrm{rain}}(L_{\mathrm{rain}} = 1)$ the received level in the absence of rain, to be used as reference for evaluating the attenuation. Then, after some manipulation, it is found that L_{rain} is given by the ratio between the received powers in the bin containing the beacon, in the absence and in the presence of rain, respectively, where each value has to be properly corrected by the rain-independent noise power contributions

$$L_{\mathrm{rain}} = \frac{P_{\mathrm{clear}} - k_{\mathrm{B}}B\left(T_{\mathrm{atm}} + T_g + T_{\mathrm{RX}}\right)}{P_{\mathrm{rain}} - k_{\mathrm{B}}B\left(T_{\mathrm{atm}} + T_g + T_{\mathrm{RX}}\right)}. \quad (7)$$

Using (7) it is possible to obtain L_{rain} from the measurement of P_{rain} and from knowledge of the reference power P_{clear} (the latter obtained from either link-budget analysis or previous measurements) and the temperatures T_{atm}, T_g and T_{RX} (the first being around 275 K, the latter two taken from the specifications of the receiving antenna and equipment). An alternative approach, as suggested in Figure 6, consists in jointly measuring both $C + N$ on the bin containing the beacon power, and N on a different bin far enough from the former containing the power peak, so that only noise can be safely measured there. The difference between the powers in the bin containing the peak and in the noise-only bin yields the value of C. This procedure is applied twice, i.e., for both the clear-sky and the rain condition, and the ratio between the values of C obtained in the two conditions will again yield L_{rain}.

For the sake of clarity, to demonstrate the potentials of the beacon-based method, let us consider the scenario described in Table 4a, where a high-power beacon signal from a Ka-band broadband service satellite is exploited and the parameter values are based on those used in [47]. The resulting performance, in both clear-sky and rain conditions (with L_{rain} = 44 dB, corresponding to a rain rate in excess of 100 mm/h over wet paths of 3-4 km at 20 GHz (see e.g. [15] (Fig. 9.7)), is presented in Table 4b. In particular, it is shown that even in this case of torrential rain, the beacon power still exceeds by around 5.4 dB the background Gaussian noise power measured within the frequency bin, thus allowing a reliable detection and estimation of the signal peak level.

Table 4. Parameters of a beacon-receiving system using a Ka-band broadband satellite: (a) system specifications (based on the numerical values used in [47]); (b) performance.

a.1	Beacon frequency	20 GHz (Ka Band)
a.2	Beacon EIRP	30 dBW
a.3	B	17 Hz

a.4	L_{FS}	210 dB	
a.5	L_{atm}	1.0 dB	
a.6	T_{atm}	275 K	
a.7	T_c	2.78 K	
a.8	T_g	10 K	
a.9	T_{RX}	100 K	
a.10	G_{R}	40 dBi	

(a)

		Clear-sky, $L_{\mathrm{rain}} = 0$ dB	
b.1	C	-111.00 dBm	Eqn. (1)
b.2	N	-164.35 dBm	Eqns. (2), (3), (4)
b.3	C/N	53.35 dB	(b.1), (b.2)
b.4	$C+N$	-111.00 dBm	(b.1), (b.2)
b.5	$(C+N)/N$	53.35 dB	(b.4), (b.2)
		Rain, $L_{\mathrm{rain}} = 44$ dB	
b.6	C	-155.00 dBm	Eqn. (1)
b.7	N	-160.44 dBm	Eqns. (2), (3), (4)
b.8	C/N	5.44 dB	(b.6), (b.7)
b.9	$C+N$	-153.91 dBm	(b.6), (b.7)
b.10	$(C+N)/N$	6.53 dB	(b.9), (b.7)

(b)

As pointed out earlier, this kind of devices are mainly proposed for systems operating in the Ka band or higher, where more powerful beacons are available [6], and seldom for the Ku band. Since COTS (i.e., commercially available off-the-shelf) devices are difficult (if not impossible at all) to find for beacon reception, practical implementations must substantially rely on *ad hoc* self-made receivers. However this additional burden is likely to pay off since, thanks to the frequency stability of beacon generators and to the consequent high resolution of the spectral analysis, these devices allow, as shown above, to measure variations of C over dynamic ranges spanning several tens of dB [47]. Therefore they allow to estimate very high values of RR (up to more than 100 mm/h).

4.1.2. SNR or ESNDR measurement on a wideband signal

In many other papers, the estimate of the RR is based on measurements made by the receiver directly on the payload signal. This is the typical case of commercial-grade receivers for the reception of TV signals in DVB-S/S2 format broadcast in the Ku band [8] or for the download streams of internet access systems operating in the Ka band or higher [5]. In these cases the conceptual scheme of the measurement system is that of Fig. 7, in which the payload signal is processed using a classic receiver chain (i.e., front end–downconversion–matched filter–sampler). The noise-corrupted samples at the output of the matched filter are sent to an algorithm that compares them with the noise-free symbols at the output of the symbol detector, and provides an estimate of ESNDR (E_s/N_0), under the assumption that the decisions on symbols are error-free. The system analyzed in [8] features an innovative device for domestic reception of satellite TV broadcasts in Ku-band, which is capable to continuously generate estimated values of E_s/N_0 and possibly retransmit them back on a return satellite channel either in the Ku or in the Ka band (more details are provided in Section 5.2.2). Another instance is in [5], discussing a specific implementation of the terrestrial terminal equipped with an estimator of the SNR. Although details of the latter are missing, it can be argued that its operation is similar to the one in [8]. In both the above papers, the proposed systems use a return channel that allows to concentrate the SNR data relevant to the received signals from the various GSs to a single centralized control station. In [8] it is shown that, for a digital transmission with symbol rate R_s, the ESNDR can be written as a function of the rain attenuation as

$$\left(\frac{E_s}{N_0}\right)_{\mathrm{rain}} (L_{\mathrm{rain}}) = \frac{\mathrm{EIRP}}{k_{\mathrm{B}} R_s L_{\mathrm{atm}} L_{\mathrm{rain}} \left[\dfrac{T_c}{L_{\mathrm{atm}} L_{\mathrm{rain}}} + T_{\mathrm{atm}} \left(1 - \dfrac{1}{L_{\mathrm{atm}} L_{\mathrm{rain}}} \right) + T_g + T_{\mathrm{RX}} \right]}. \qquad (8)$$

398 Denoting as $\left(E_s/N_0\right)_{\text{clear}} = \left(E_s/N_0\right)_{\text{rain}} \left(L_{\text{rain}} = 1\right)$ the ESNDR in clear-sky conditions, we obtain the following expression
399 for the rain attenuation

$$L_{\text{rain}} = \frac{\left(E_s/N_0\right)_{\text{clear}}}{\left(E_s/N_0\right)_{\text{rain}}} \left(1 - \xi\right) + \xi, \tag{9}$$

401 where we defined

$$\xi = \frac{T_{\text{atm}} - T_{\text{c}}}{L_{\text{atm}} \left(T_{\text{atm}} + T_{\text{g}} + T_{\text{RX}}\right)}. \tag{10}$$

403 This type of approach can be easily pursued since the market offers low-cost COTS receivers capable to perform SNR
404 or ESNDR estimates and, as noted earlier, some of them are also equipped with a return channel [8], [5].
405
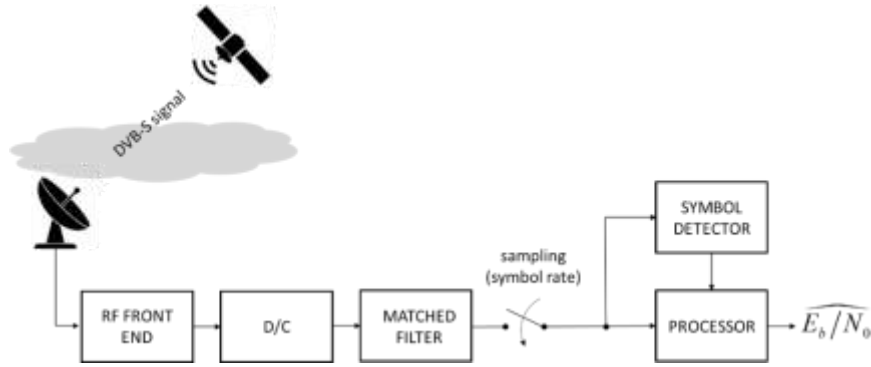
408 **Figure 7**. High-level block diagram of a broadband signal receiver (e.g., DVB-S) for the estimate of the ESNDR.

409 *4.2. Mapping of rain attenuation onto rainfall rate and related issues*

410 4.2.1. General procedure for mapping

411   As previously pointed out, the attenuation L_{rain} introduced by the rain on the received signal is an integral value
412 depending on the particular distribution of the rain field along the "wet segment" of the satellite - GS radio path (see
413 Figure 1). This implies that, in general, the knowledge of L_{rain} alone is not enough for the retrieval of the RR in the
414 proximity of the receiver. However, if we add the assumption that the RR is approximately constant on the aforemen-
415 tioned wet segment, the problem of estimating RR at the receiver can be easily solved provided the length of the wet
416 segment is known. Actually, by dividing L_{rain} (expressed in dB) by the length L_s of the wet path (in km), we find the
417 specific attenuation *k* (in dB/km)

$$k = \frac{L_{\text{rain}}}{L_s} \ \ (\text{dB/km}) \tag{11}$$

419 which is expressed by (5) as a function of the RR. In the simple precipitation model of Figure 1, the length of the wet
420 path can be obtained from the elevation angle θ of the GS antenna and the rain height w.r.t. the level of the GS, $h_R - h_S$
421 , as follows:

$$L_s = \frac{h_R - h_S}{\sin \theta}, \tag{12}$$

423 Also assuming that the coefficients *a* and *b* are known, inversion of (5) eventually yields an estimate of the RR.

424 4.2.2. Melting Layer effects

425   A more accurate RR retrieval procedure can be implemented by specifically considering the impact of the ML.
426 Recalling the discussion in Section 2.2.2, a possible approach is to adopt the precipitation model illustrated in Figure 4
427 and to ascribe to the LL and to the ML separate contributions to the overall attenuation L_{rain}, both based on power-laws
428 as in (5) when expressed in logarithmic form, but with coefficients specifically calibrated for each layer. The global
429 (logarithmic) attenuation is the sum of these two contributions. When following this procedure, the two cited contribu-

430 tions summing up to L_{rain} must be expressed as a function of the RR present in the LL, and subsequently the relation-
431 ship must be inverted so as to provide the RR corresponding to a global measured logarithmic attenuation (see [8] (sect.
432 V) for an example). Alternatively, we could retain the simple single-layer model in Figure 1, where the height of the
433 rain is fictitiously modified by purposely adding a corrective term to the 0 °C isotherm height as recommended in [52].
434 By this way, we are reverted to a single-layer model, but with an extended wet segment, which produces an additional
435 attenuation equivalent to that of the ML. In this case the inversion procedure is facilitated as we have to deal with a
436 single power-law term. Some further details on these issues are in Sections 5.4.1 and 5.4.2.

437 4.2.3. Non-uniformity of the rain and geometrical issues

438 The assumption of uniform rain distribution along the whole length of the wet segment may actually prove unre-
439 alistic in many cases. Even if we model the precipitation field structure as one or more spatially-separated, cylindrically-
440 shaped rain cell(s) with uniform RR inside (as shown in Figure 8), the intercept of the cell(s) and the slant path $\overline{op}$ will
441 typically affect just a part of the path itself. The problem of a possible non-uniformity of the rain field along the wet
442 segment is tackled in [53] where the accuracy of the RR estimate at the receiver, obtained from a single-layer model, is
443 improved by applying a corrective coefficient to the value of L_{rain}. Besides the usual geometrical parameters of the link
444 (i.e., length of the wet segment and antenna elevation angle), this coefficient also takes into account the following fea-
445 tures:

446 the diameter of a single (cylindrically-shaped) rain cell;
447 the average length of the intercept of the projected slant path with the randomly positioned circles representing the
448 ground projection of multiple rain cells;
449 a calibration coefficient which takes into account the non-uniform distribution of rain inside the cell.
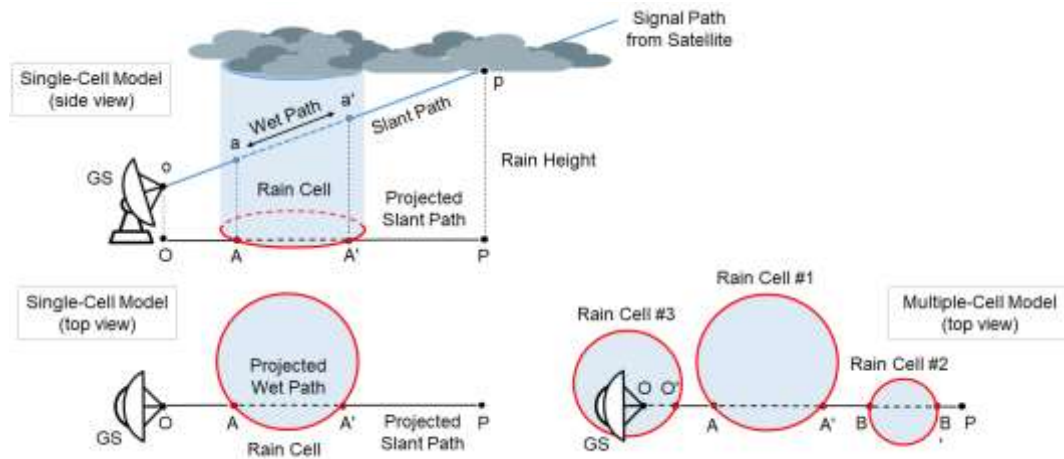450

453 **Figure 8**. Precipitation modeled as one, or more cylindrically-shaped rain cell(s) with uniform RR inside.

454 **5. Survey of Rainfall Rate Estimation Techniques**

455 Many opportunistic techniques for RR estimation by means of satellite receivers are available in the literature. As al-
456 ready mentioned, the various techniques are characterized by a variety of solutions and features that will be addressed
457 hereafter in greater detail, namely with respect to:

458 *i)* satellite orbit and downlink frequency band (Section 5.1);
459 *ii)* physical quantity to measure, generically termed as the "strength" of the received signal, to be processed for estimating
460 the RR, and type of receiver (Section 5.2);
461 *iii)* type of processing (Section 5.3) for:
462 the detection of a rain event, together with the relevant start and end epochs;
463 identifying the "baseline" signal strength in the absence of rain ("clear-sky"), to be used for evaluating the signal
464 strength reduction during rain events;
465 obtaining the estimate of RR from the measurement of signal strength reduction;
466 *iv)* ancillary information (geometric, climatic and meteorological) required by the RR estimation algorithm and how to
467 collect it (Section 5.4);

468) techniques to recognize and tackle sudden strength variations of the signal strength, not due to rain (Section 5.5).

5.1. Type of satellites

5.1.1. Satellite orbits and frequency bands

The vast majority of the systems cited in the bibliography refers to the use of one or more GEO satellites, but some solutions have also been proposed, especially in recent times, for the case of LEO satellite constellations belonging to global mobile communication networks [17], [18]. With reference to Table 2, the downlink frequencies associated with the GEO broadcasting satellites are mostly in Ku band, plus a minor slot in the Ka band, while broadband communication satellites, either for fixed (GEO) and mobile (LEO) services, operate exclusively in Ka band. In the recent years, the growing demand for higher throughput stimulated research and experimentation in the spectrum above 30 GHz (the Q/V band) [54], [55]. From the perspective of the opportunistic approach to rain measurement, this migration from Ku to Ka, and then to Q/V, is a really appealing opportunity, because the higher the frequency, the greater is the effect of rain attenuation and the more easily it can be measured.

5.1.2. Tomographic approaches and other techniques for the reconstruction of the precipitation fields

A GEO satellite is seen from terrestrial terminals under a constant azimuth angle which depends on the (fixed) longitude of the satellite. Consequently, in order to probe the rain field along other directions, it is necessary to resort to the joint reception of several GEO satellites, positioned over a sufficiently wide arc of longitudes [50], [54], [55], [56]. Tomographic techniques have been therefore proposed for estimating the rain fields on a territory covered by several geographically distributed receivers and/or by using multi-antenna GSs capable of simultaneously receiving at the same site several satellites visible on different azimuth and elevation angles. This type of techniques can, in principle, provide the most accurate estimation of non-uniform rain fields at ground level. In case of LEO constellations, instead, the mobility of the satellites across the sky allows to probe the volume affected by the rain in several directions, and therefore lends itself to the use of tomographic techniques much more easily than for GEO [17], [54], [55]. In fact, a terrestrial terminal sees each single LEO satellite to scan a wide range of azimuth angles as the satellite moves (except in the particular case in which the satellite ground track passes exactly on the point where the terminal is located; in this case the terrestrial terminal sees the satellites under a constant azimuth and with an elevation from $0°$ up to $90°$ and then down again to $0°$).

It is worth remarking that all of the currently available prototypes operate with GEO satellites only, while the utilization of LEO signals remains thus far at the level of feasibility studies, and therefore will not be further pursued in the following.

5.2. Measurement of signal level at the receiver and related hardware issues

All the proposed RR estimation algorithms are based on the monitoring of a performance measure of the received signal, such as the signal power level, or the SNR, or the ESNDR, and on the evaluation of its reduction caused by rain compared to clear-sky conditions. The knowledge of this reduction of the performance measure allows to evaluate the attenuation introduced by the rain on the radio link and eventually to estimate the corresponding RR.

5.2.1. Beacon-based approach

One of the most used techniques consists of measuring the level of the unmodulated beacon signal transmitted by the satellite, and evaluating the attenuation due to rain by means of the procedure outlined in Section 3.3.1, where Figure 6 details the required signal processing. As discussed in Section 3.3.1, this technique allows to obtain a good measurement dynamic range thanks to the possibility of using a very narrow band filter for the detection of the beacon signal. By this way, in clear-sky conditions, it is possible to obtain very high SNRs (tens of dB) which enable a wide dynamic range in the measurement of the rain attenuation and in the estimates of RR (many tens mm/h or more). Use of higher frequency bands, such as the Ka or the Q band, can further improve the sensitivity of the algorithm to rain as demonstrated in [50], [54], [55].

Some of the solutions available in the literature produce estimates of the RR directly from the measurement of the variation of the overall received power, apparently ignoring the effect of the rain noise (for example [50], [54], seem to adhere to this simplified approach).

Most works instead illustrate in detail the whole signal processing chain, starting from the measurement of the total power at the receiver prefilter output and producing the estimate of the beacon power after removing the effect of noise (e.g. see discussion in Section 4.1.1). The latter approach is expected to yield better accuracy at low SNR values, especially when the attenuation due to rain (and therefore the impact of the relevant noise) is severe.

A common feature of beacon-based RR estimators is the need of a custom hardware realization of the beacon receiver/meter device which can render this approach quite onerous, especially if compared with COTS-based solutions

520 (see hereafter). This raises serious doubts about the feasibility of a wide network of sensors of this type, with a reason-
521 able effort.

522 5.2.2. COTS-receiver-based approach – Ku band

523 A promising and cheaper alternative relies on low-cost COTS terminals, commonly known as set-top boxes (STBs),
524 which are already installed in millions of domestic premises worldwide for the reception of DTH TV broadcasts from
525 GEO satellites, mainly in the Ku band. STBs are typically receive-only devices, and the return channel, when available,
526 reaches the broadcaster only via the internet network. Any STB has some signal strength meter functionality for system
527 set-up, parabola aiming and diagnostic purposes which could, in principle, provide useful material for RR estimation.
528 Unfortunately, accessing those data may reveal a harsh (if not impossible at all) task for most of the COTS terminals.
529 Things are much easier in case of "open" receivers, i.e., based on the open-source Linux operating system, where a
530 skilled user, via ethernet interfacing, can upgrade the firmware and read the receiver internal status, including received
531 signal strength. Furthermore, a next-generation of interactive satellite terminals has been recently launched in the mar-
532 ket and could gradually replace the equipment currently employed for satellite TV reception. This novel device, com-
533 mercially branded by Eutelsat as "SmartLNB" [8], has the appearance of a common LNB (Low-Noise Block, i.e., the
534 outdoor unit mounted in the focus of the parabolic reflector), but it exhibits some remarkable innovative features,
535 namely: *a*) it is only slightly larger than a conventional LNB, but it integrates within its case all functions of both the
536 LNB and the decoder (i.e., the indoor unit which is placed next to the TV set or directly integrated in it), thus represent-
537 ing a complete and compact DTH satellite receive system; *b*) it performs an accurate real-time monitoring of the received
538 signal quality, by producing frequent estimates of the ESNDR (typically, one estimate per minute), as shown in Figure
539 7; *c*) it is a two-way device that includes also a low-power transmitter enabling a low-data-rate packed-based return
540 channel, i.e., an RF link from the user premises (in the Ku or Ka band), via the same GEO satellite, to a Service Center
541 (SC) in charge of collecting and processing user data [57] for pay-per-view, social networking, live interaction, subscrip-
542 tion management, audience meter, and IoT (Internet of Things) services.

543 The features in *b*) and *c*) make the SmartLNB a very appealing satellite receiving equipment for opportunistic RR meas-
544 urements. Actually, the ESNDR readings are encapsulated, together with other information about the device status, into
545 the return channel data stream and, without the need for any terrestrial communication infrastructure, are sent via
546 satellite to the SC, where they can potentially feed the RR estimation algorithm. So, thanks to both its embedded ESNDR
547 estimator and built-in transmitter, any SmartLNB for domestic satellite reception can also be seen as a signal strength
548 meter equipped with a modem for wireless data collection, and this works from any location within the area covered
549 by the GEO satellite. Furthermore, a single GEO satellite for TV broadcasting typically serves many countries or even a
550 whole continent; for instance, Eutelsat's Ku band satellites located at 10°, 13° and 16° East cover all the European conti-
551 nent (plus surrounding areas such as North Africa, the Mediterranean basin, the Anatolian Peninsula and inner Russia).
552 This means that any GEO satellite has a potential audience of several millions domestic DTH receivers that are also
553 prospectively all measurement sites. The possible collisions among the huge number of packets arriving at the SC via
554 the return link are effectively tackled and solved thanks to a high performance Random Access protocol dubbed En-
555 hanced Spread Spectrum Aloha (E-SSA), especially conceived for packet-based return link in satellite applications and
556 featuring Successive Interference Cancellation (SIC) techniques. It is shown that, due to jointly a robust rate in the turbo
557 encoder and to the iterative cancellations, the packet collisions do not affect the system performance [58].

558 This enables the construction of rain maps, reasonably on regional, but also on even broader scale, where each terminal
559 corresponds to a point on the map, and whose spatial resolution is related to the density of terminals installed on the
560 territory.

561 An approach based on Eutelsat's SmartLNB receivers was studied in the framework of the Nefocast project (funded by
562 regional administration of Tuscany, Italy), as discussed in [3], [8].

563 Anyway, once the ESNDR readings are somehow made available for processing, either using properly-interfaced open
564 STBs or SmartLNBs, the RR estimation algorithm operates in the same manner. That is, the ESNDR is continuously
565 tracked and compared with a clear-sky reference level, which can be pre-stored at the initial set-up or adaptively up-
566 graded from previous days measurements. When a rain fade is detected, the corresponding attenuation is analytically
567 derived from (9). Then, the specific rain attenuation k (in dB/km) in the LL can be obtained by resorting to the tropo-
568 spheric model in Figure 1, and the instantaneous RR value is eventually achieved by inverting the power-law in (5).
569 Alternatively, the effect of the ML can be taken into account, by means of improved precipitation inversion models, like
570 that in [8] which is based on the three-layer model in Figure 4, or that in [40].

571 A possible point of weakness for a system of this type is related to the dynamic range it offers for the measurement of
572 the ESNDR. Actually, the rain margin of these satellite downlinks is tailored for the peculiar service they are intended
573 to (i.e., TV broadcast or broadband internet), so that intense precipitations may cause service outage with a given non-

negligible probability, set by design specifications. Accordingly, in a practical implementation of the system, the nominal value of ESNDR at the receiver with standard reception equipment and in clear-sky conditions is typically chosen with a few (say 5-6) dB of margin above the minimum required threshold ESNDR (set by the selected signal mod/cod, see Section 2.2), below which the receiver incurs outage. For instance, the experimental setup described in [8] uses the downlink of the EUTELSAT 10A satellite with a link margin of around 5.8 dB (see the parameters in Table 3). Most of the receiver ESNDR estimators rely on carrier and clock synchronization, and therefore during the outage caused by heavy rain, they are unable to provide any useful estimate (however, there are also some receivers that are capable of estimating values of ESNDR below the mod/cod threshold). Though tolerable for the intended broadcast or broadband services, link breakdowns inhibit detection and measurement of the most intense precipitations, which are instead the most interesting ones from the perspective of a rain monitoring system. The resulting dynamic ranges offered by COTS devices for estimating rain attenuation turn out to be limited to a few tens of mm/h, as confirmed by Figure 9 which refers to the algorithm described in [8] and presents the estimates of the RR vs. the ESNDR within the receiver operating range, from 4.68 dB (minimum required value for the selected mod/cod) to 10.5 dB (nominal received level in clear-sky conditions). As is apparent, even with some sensitivity to the value of the 0 ºC isotherm height, the maximum RR that can be measured is around 30 mm/h. Just to give an idea of what this value represents in terms of probability, let us consider the table of rainfall intensity for the world rain climatic zones in ITU-R recommendation 837-1 [59] (we refer to this superseded recommendation for the sake of exemplification only). In region "L", which includes Western Tuscany (Italy) where the experiments of [8] have been carried out, the RR is shown to exceed 33 mm/h with a probability of 0.03%. This means that, during one year, the received ESNDR falls below the threshold 4.68 dB for approximately 160 minutes, i.e. 2h 20', overall, and this is also the total duration of outages which could inhibit RR measurements.
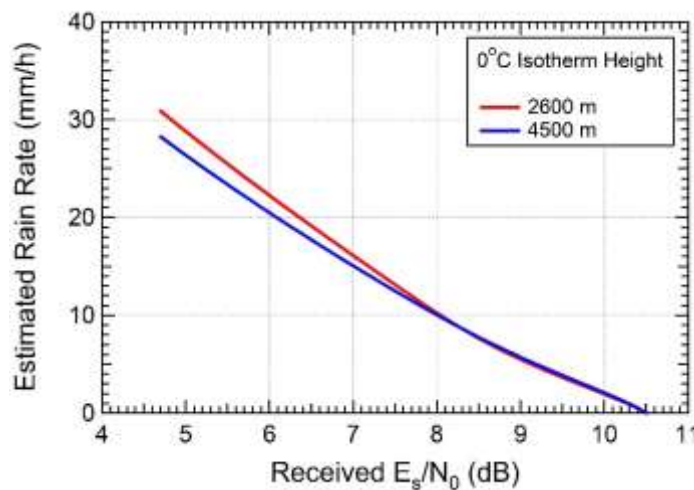

Figure 9. Dynamic range of the RR estimation technique in [8], with 10.5 dB of nominal clear-sky ESNDR and 4.68 dB of minimum required ESNDR (see Table 3).

5.2.3. COTS-receiver-based approach – Ka band

A system similar to the previous one and operating in the Ka band is proposed in [5], where a method is discussed allowing estimation of RR from measurements of the received SNR taken at constant rate (one every 5') on a broadband payload signal transmitted by an existing broadcast satellite. The paper does not provide details on how the SNR observations are mapped onto values of rain attenuation undergone by the satellite signal, nor does it describe the relationship existing between the SNR and the RR. In particular it gives no hints on how the noise power is related to rain intensity. In any case, [5] confirms that the SNR margin available for rain estimation is very narrow, since the baseline SNR is designed so as to guarantee a satisfactory quality of the received signal in the nominal dry operating conditions, with an edge of only a few dB over the outage limit. Consequently, the range of measurable RRs is very small and does hardly exceed 10 mm/h. As discussed in Section 4.1, a viable and reliable route to achieve a wider dynamic range for signal attenuation is to resort to systems measuring the level of calibrated narrowband beacon sources.

5.3. Processing issues

The performance of a RR estimation algorithm based on measurements of downlink SNR or ESNDR is strictly related to the specific criteria utilized to implement the numerous functions and processing steps involved in the algorithm. We hereby provide a short overview of the relevant issues.

5.3.1. Identification of the rainy periods

A particularly crucial issue is the identification of the starting and ending instants of the time intervals within which the received signal incurs a level reduction actually due to the presence of rain on the satellite – GS radio path. The problem cannot be solved in a trivial way in view of the large number of possible rain-independent factors that can cause a drop in the signal level, as discussed in Section 3.1, and a good algorithm should be able to distinguish the effect of rain from those imputable to other causes.

In general, all algorithms proposed in the literature are designed to be insensitive to fast fluctuations due to ionospheric scintillation, as the raw SNR or ESNDR measurements are usually smoothed out at some early processing stage by a low-pass filter calibrated on the time variability properties of the rain attenuation process, which is a far slower phenomenon than scintillation. Moreover, in order to reliably recognize the rain-induced signal level variations, it is necessary to identify and compensate for the slow signal fluctuations deriving from oscillations and drifts of the satellite position or from power/attitude corrections (Section 3.1.2), which can be misinterpreted as rain effects. We return on these issues further below.

The techniques devised to recognize the start and stop instants of a rain event are numerous and characterized by different levels of complexity. A straightforward albeit rather simplistic approach involves the preventive estimation of the dry baseline level by averaging measurements of SNR or ESNDR over very long time intervals (order of days), followed by the choice of a rain detection threshold, adequately lower than the above dry baseline to reduce the risk of false detections (normally at least 1 dB down). The presence of rain is declared when the sequence of measurements drops below this threshold, and conversely the dry condition is assumed when it is above. The baseline level can be continuously updated offline during dry periods. To limit the incidence of false rain detections, the distance between the baseline and the threshold must be such not to be affected by the slow SNR/ESNDR fluctuations mentioned above, which can significantly reduce the sensitivity of the algorithm, making it unable to detect small intensity rains. Furthermore, depending on how the low-pass filter for smoothing out fast fluctuations is designed, a delay in rain detection may be introduced not always compatible with the real-time response requirement of certain applications. For instance, in [1], [6], [49] sliding window filters are used with response latency in the order of tens of minutes.

In [3], [8] the dry baseline against which to compare the series of SNR or ESNDR values is updated in real time, through the use of a "slow" Kalman tracker, featuring a very long time constant in comparison with the typical length of fluctuations induced by rain events (and even more so with respect to scintillation). Its output during dry periods faithfully reproduces the trend of very slow fluctuations such as those due to satellite oscillations and station keeping maneuvers. In parallel to this device, a second Kalman tracker operates with a faster response which, while removing the fluctuations due to scintillation, is able to track with negligible delay the variations of SNR/ESNDR at the occurrence of a rain event. Therefore, while in the dry state the two trackers have almost coincident outputs, a rain onset event produces a sudden deviation (in reduction) of the fast tracker output compared to the slow one which, due to its inertia, remains insensitive to rain for a few minutes. Conversely, end of rain is identified by the fast tracker returning close to the baseline level, the latter determined during the wet periods as discussed in the next Section 5.3.2. Due to this "adaptive" nature of the algorithm, the distance of the rain detection threshold from the baseline can be reduced down to a small fraction of a dB (e.g., 0.3 dB) and therefore the algorithm allows a sensitivity gain compared to the systems described earlier.

A still different and more elaborate approach [5] consists of modeling the slow daily fluctuations affecting the SNR/ESNDR in the dry state as sinusoidal (see the example in Figure 3), followed by estimating the parameters of this sinusoid and eventually proceeding to its preventive cancellation from the sequence of observations. The purpose of this procedure is to obtain after the above cancellation a substantially constant dry baseline against which to measure the deviations of the current SNR/ESNDR during rainy periods. The latter are recognized in [5] by means of a neural network operating on the basis of the different statistical behavior (notably the more pronounced fluctuations) exhibited by the SNR/ESNDR time series in rainy periods compared to dry conditions. The cited paper does not discuss how the RR estimates are impacted whenever the aforementioned sinusoidal model fails, for example during station keeping adjustments. Furthermore, the need to previously estimate and remove the periodic fluctuation from the input data seems hardly compatible with the algorithm capability to operate in real time.

Besides [5], other authors [1], [40] have investigated the use of an appropriately trained neural network to identify rainy periods, geared to analyze, recognize and classify the statistical behavior of the received signal. This category of techniques appears promising even though at the moment it does not seem clearly demonstrated that it is definitely more

advantageous than other more traditional methods, particularly with regard to the accuracy achievable in identifying the instants of start and stop of a rain event. Also to be mentioned, [8] proposes a technique having the same purpose as the neural network in [5], although conceptually simpler. In fact in [8], immediately after the detection of rain by means of the double slow/fast Kalman tracker mentioned earlier, a confirmation of this rain event is sought by estimating the dispersion of the current SNR/ESNDR fluctuations around their average, and then, on the basis of these statistics, taking a decision about the actual presence of rain.

Finally, we mention the approach adopted in [4], [7] to recognize rainy periods, based on a metric related to the receiver bit error rate (BER), a parameter provided by most domestic satellite receivers. Here the underlying idea is, since the receiver BER is univoquely related to the current SNR/ESNDR, then it is possible to infer the presence of rain by monitoring the BER. However this technique leaves some doubts about the sensitivity in detecting small RRs, and also in the ability to counteract the slow variations of signal level discussed in Section 3.1.2.

5.3.2. Identification of the dry baseline during dry and rainy periods

The problem of identifying the dry baseline to be used as reference level against which to measure variations of SNR or ESNDR must be addressed differently depending on whether we assume to carry out the above identification in the absence or presence of rain. In the former case, it is sufficient to accurately track the SNR or ESNDR (and its possible evolutions, as discussed Section 3.1), waiting for a rain event to occur. This task appears fairly straightforward since in the absence of rain the desired baseline value is "embedded" in the received signal as actual SNR or ESNDR, and it is sufficient to perform a conventional estimation of this parameter minimizing the effect of noise and of the other occasional impairments mentioned in Section 2.1.

Conversely, during a precipitation event the dry baseline SNR or ESNDR is no longer embedded in the received signal, making it necessary to figure out the hypothetical value that would be taken on by this parameter if it did not rain. This parameter is crucial for the algorithm operation, since it serves as reference level against which to assess the attenuation induced by rain. Obviously the latter task is more difficult than the former and its solution necessarily passes through a sort of "guess" of the dry baseline, as this parameter is not observable during rain.

Furthermore, while this guess is certainly accurate at the very start of the rain event, when the dry baseline cannot deviate much from the value assumed immediately before rain inception, conversely over a long period of uninterrupted rain (say in the order of tens of minutes and more) the actual current (unknown) dry baseline may depart significantly from its initial value, and therefore it becomes appropriate to try to figure out what its actual evolution would be, using all the available *a priori* information about its behavior.

As for the determination of the dry baseline in the dry periods, in the previous section we have already provided a review of the main techniques proposed in the literature to carry out this task [1], [5], [8], [49]. They differ from one another mainly for the various approaches devised to counteract the slow fluctuations affecting the measurements of the performance parameter under the dry state assumption.

Turning to the determination of the dry baseline in rainy periods, there is a variety of approaches proposed in the literature. As already mentioned, some authors [1] use a fixed or very slowly varying baseline during both dry and rainy periods, obtained from a long-term average of dry-state measurements. This type of approach is conceptually simple, but not very accurate since to avoid false rain detections the chosen reference level has to cut out the daily fluctuations due to the satellite motion (Section 3.1), and therefore it is hardly sensitive to small RRs. Furthermore, in [5] where, as already seen, the dry baseline is obtained by canceling the periodic daily component from the series of SNR measurements taken in the dry periods, at rain inception this baseline is "frozen" and used as a constant reference for the entire rain event, regardless of its duration and without taking into account any fluctuations in the dry reference that may occur during the rain. This approach may in fact lead to growing errors as the rain event goes on.

In other cases [5], [54] the dry baseline during rainy periods is obtained by linearly interpolating between the two measured dry levels immediately preceding and following the rain event. It is observed that this type of off-line approach is not compatible with real-time operation of the RR estimator since the aforementioned interpolation of the baseline requires that the end of rain is waited for.

A further variant is in [3], [8], where at the onset of a rainy period the last dry baseline provided by the aforementioned slow Kalman tracker (Section 5.3.1) is used as the initial reference, thence the slow Kalman tracker is stopped and the RR estimation algorithm proceeds using as reference the dry baseline values utilized the previous day at the same time that have been stored in memory. The data drawn from the previous day are corrected by adding a fixed shift (accounting for a possible long-term drift of the baseline) so as fit them to the dry-state measurements available up to the rain event, avoiding any discontinuities. In so doing, the most likely inherent daily fluctuations of the baseline are taken into account even while it rains, improving the real-time operation of the algorithm.

5.3.3. Rainfall rate estimation and comparison with rain gauges

719 All algorithms proposed for RR estimation pass through the determination of the specific attenuation k (dB/km) char-
720 acterizing the wet segment of the satellite-GS path and related to RR by (5), where the values of the coefficients a and b
721 are determined as discussed in Section 3.2.1. Several authors [5], [3] adhere to the recommendations [36] which provide
722 typical values for a and b, while others employ values deriving from dedicated experimental campaigns carried out in
723 specific areas of interest, possibly with the use of disdrometers [37], [60], and are therefore to be considered more accu-
724 rate for the above geographical areas.

725 Furthermore, most papers deal with the problem of comparing the RR data resulting from satellite signal attenuation
726 with those coming from conventional rain gauges. In general, these two rain measuring techniques are not exactly com-
727 parable, even when the rain gauge is placed in close proximity to the satellite receiver. This is true in view of at least
728 two types of arguments: on the one hand, the variation of the received signal power with respect to the baseline is
729 related to the *instantaneous* distribution of RR present on the wet segment of the radio path, while the rain gauge by its
730 nature provides a measure of the *cumulated* (integrated) rainfall over a certain (albeit possibly short) period of time. It
731 is noted that in order to make the two measurements homogeneous, many authors refer to cumulative pluviometric
732 readings carried out at a fixed time spacing (e.g., one every 5') and compare them with the instantaneous RR measure-
733 ments produced by the satellite receiver integrated for the same period of time.

734 On the other hand, the rain gauge produces point-scale measurements, i.e. it provides information about the rain actu-
735 ally fallen during the intended time interval precisely at the rain gauge site, while the power reduction experienced by
736 the GS is the overall effect of rain on the entire wet segment of the satellite-GS radio path, along which the RR is not
737 necessarily constant, and it therefore leads to a sort of "average" RR on the wet segment.

738 The different inherent operation of the above two sensors may sometimes lead to conflicting indications about rainfall
739 presence and intensity. For example, it may happen that the satellite receiver perceives a signal level reduction when it
740 is not yet raining over the GS site and, vice versa, the rain gauge may start detecting raindrops when the precipitation
741 does not yet significantly impact the received power. In any case, experience shows that the above effects can be ignored
742 to a first approximation when the horizontal projection of the radio path wet segment (whose length is $L_s \cos\theta$ from
743 Figure 1) is of the same order or shorter than the rain cell extension, which is after all a rather common situation. In any
744 case, the impact of non-uniform rain distribution on the performance of the satellite system can be mitigated through
745 application of adequate corrective coefficients when mapping the measured rain attenuation L_{rain} on an estimate of RR
746 (Section 4.2.3).

747 Further improvements of the RR estimation accuracy in the vicinity of the receiver site can be achieved if it is possible
748 to build a 2D geographic map of the rain field through joint processing of the data collected from multiple terminals
749 scattered throughout the area. This type of approach permits in fact to evaluate the RR gradient on the wet segment of
750 the radio path (see also discussion in Section 4.2.4).

751 5.3.4. Latency issues

752 Another aspect in which the proposed algorithms may significantly differ from one another is their capability to pro-
753 duce the RR data in (almost) real time. This issue is important in view of the possible use of these techniques in support
754 of surveillance and early alert infrastructure deployed to counteract potentially dangerous weather events. Some au-
755 thors demonstrate specific awareness and attention to this problem: for example, the approach discussed in [5], [54] is
756 based on a neural network purposely designed for the detection of rain with a negligible delay, so as to meet the re-
757 quirements of real-time operation. Rather curiously, to obtain the SNR baseline during a rain event, the algorithms use
758 interpolation of the dry-state baseline measured at start and stop of rain, a requirement that seems hardly compatible
759 with real-time operation (see also Section 4.3.2). A similar observation can be made about the algorithm in [5] already
760 discussed in Section 3.3.2, regarding the possible incompatibility with real-time operation of the prior removal of the
761 periodic component from the input data. In many other papers [1], [5] more focused on demonstrating the feasibility of
762 RR estimation through the exploitation of a satellite link, the issue of latency is not central to the paper scope and is
763 therefore ignored.

764 *5.4. Ancillary information required by the RR estimation algorithm*

765 5.4.1. Rain height vs. 0°C isotherm height

766 All of the algorithms discussed so far require knowledge of the rain height to determine the length of the wet segment
767 on the radio path (Section 4.2.1). With reference to a stratiform precipitation, this height is closely related to the altitude
768 h_0 of the 0° C isotherm [61]-[67], which in its turn can be identified in three ways.

769 The first, and the most accurate one, consists in relying on an external source (typically a weather service agency)
770 providing actual measurements of h_0 generated by radar sensors or, accepting a slightly lower performance, on short-

771   term forecasts of h_0 made by a numerical weather prediction (NWP) method, such as the Weather Research and Fore-
772   casting (WRF) model developed by LaMMA Consortium, based in Florence, Italy (www.lamma.rete.toscana.it/en).
773   The second way, consists in setting h_0 as the daily average obtained from some public-domain database containing
774   the recordings of the 0°C isotherm height over a significantly large number of years, for the site where the receiver is
775   installed, such as NASA's Modern-Era Retrospective analysis for Research and Applications (MERRA) database
776   (gmao.gsfc.nasa.gov/reanalysis/MERRA) [68]. This average/typical value of h_0 is then used to identify the rain height
777   $h_R - h_S$ (see also discussion in Section 3.2), which finally through substitution in (11)-(12) permits to calculate the spe-
778   cific attenuation. This method sacrifices some performance, since it is clearly affected by errors resulting from the ran-
779   dom fluctuations of the actual value of h_0 with respect to the statistical data reported in the database. However, it
780   greatly simplifies the implementation as it requires only the availability of the, site-specific, pre-calculated set of 365
781   daily averages, without any connection to external databases.
782   A third, though rather crude, approximation consists in assigning to h_0 a constant value given by the yearly average
783   of the 0°C isotherm height, provided from ITU-R's recommendation P.839-4 (www.itu.int). Clearly, this method further
784   sacrifices performance, but it is also the easiest to implement as it requires only the knowledge of a constant, site-specific,
785   value.
786   Once the value of h_0 has been identified, it is possible to proceed to the determination of the rain height to be used in
787   (11)-(12) for calculation of the specific attenuation. Actually, the rain height rarely coincides with h_0 in view of the
788   existence of the ML, where ice particles coexist with raindrops, which itself is responsible for part of the signal attenu-
789   ation. As pointed out in Section 3.2, to obtain an accurate estimate of the specific attenuation to be ascribed only to the
790   liquid phase layer, it would be necessary to know both the attenuation introduced globally by the ML (which attenuates
791   in a different way compared to the LL) and its vertical thickness (usually in the order of hundreds of meters) to be
792   subtracted from h_0, and this task appears quite challenging in terms of type, number and cost of weather sensors re-
793   quired.
794   A less accurate model but easier to implement is to consider the ML absent, adopting an *equivalent* liquid rainfall height
795   (usually higher than the real one), to which the entire attenuation of the signal is ascribed, including that due to the
796   suppressed ML. This type of approach, preferred by most authors, is also suggested in [52], where it is recommended
797   to assume an equivalent rain height equal to h_0 augmented by the fixed amount of 0.36 km. There are also some papers
798   [69] in which the rain height is assumed to coincide with that of the lower edge of the clouds, that can be measured with
799   weather sensors.

800   5.4.2. Impact of the melting layer

801   Some papers investigate in greater detail the impact of the ML (see Sections 3.2.2 and 4.2.2), by proposing models to
802   calculate its contribution to the attenuation, as distinct from that due to the entirely liquid layer. Papers [32], [34], widely
803   cited in the literature, propose to treat the ML in the same way as the LL, by fictitiously characterizing it by a constant
804   RR equal to that in the LL as the altitude varies, with specific attenuation still given by an expression of the type (5),
805   albeit with coefficients *a* and *b* different from those used in the LL, and such as to generate the actual attenuation of the
806   ML. In [8] a variant of this method is proposed, wherein the specific attenuation model (5) is applied to elementary
807   horizontal slices of ML, characterized by a liquid fraction varying linearly with altitude as in one of the models assumed
808   in [32], starting from 0 mm/h at h_0 and ending up to the full RR value of the LL at the lower edge of the ML. As for the
809   ML vertical thickness, it is obtained either from measurements carried out by means of a weather sensor [8], or provided
810   by some short-term weather forecasting agency or, again, drawn from a statistical database as an average or typical
811   value. During an experimental campaign carried out in Rome (Italy) [70], the signature of the melting layer was obtained
812   with a dual-polarization radar. Polarimetric measurements at vertical incidence showed that the vertical extent of the
813   ML ranges between 150 and 600 m. Accordingly, in the practical implementation of the Nefocast algorithm for RR
814   estimation, the thickness of the ML was assumed as 500 m. To be finally noted, in [8] it is shown that this RR estimation
815   technique is weakly affected by (even large) errors in the knowledge of the ML thickness.

816   *5.5. Sudden variations of signal level due to causes different from rain*

817   5.5.1. Sun blinding

818   The sun blinding effect consists of an abrupt growth of the noise level due to the passage of the sun near the pointing
819   direction of the GS antenna, and is mentioned in Section 3.1.3 as one of the possible impairments of the downlink,
820   occasionally being so severe as to cause link outage. However due to its marginal and sporadic impact on the signal
821   quality it is substantially disregarded in the references of interest here. As already noted, the solar outage events are
822   deterministic (although their intensity and duration depend on the gain of the ground antenna, i.e. on the angular width

823 of the main lobe in its radiation pattern), and signal segments affected by this phenomenon can be predicted very accu-
824 rately, allowing to momentarily suspend the RR detection and estimation algorithms in these intervals. The gaps that
825 these events leave in the sequence of measurements have a short duration (a few minutes), so it seems reasonable in the
826 meantime to keep the dry baseline fixed at the last value assumed prior the sun transit for the whole duration of the
827 fade event, as suggested in [8]. It is also observed that during a sun transit both the received power and the SNR vary
828 in a smooth and almost deterministic way (see Figure 3), so it can be argued that automatic rain detection algorithms
829 based on the analysis of the measurement statistics, such as for example those who use neural networks, would be able
830 to correctly classify the event as non-rainy.

831 5.5.2. Operator corrections

832 This impairment factor is mentioned in Section 3.1.4. Similarly to sun blinding events, the operator's corrections of
833 satellite transmission and satellite kinematic parameters may entail large and sudden variations of the received power
834 but, unlike sun passages, the latter kind of events are not predictable in terms of time of occurrence, nor in their intensity
835 and (increase/decrease) sign. However, to recognize this type of events it seems possible to resort to techniques, already
836 mentioned in the previous section, based on the use of a neural network for the classification of signal statistics. This
837 type of techniques, as already seen, have been proposed to recognize the rain/no rain state by analyzing the behavior of
838 the received signal [5]: if the neural network, following a sudden change in the signal level, does not recognize the
839 statistical behavior typically induced by rain, after a relatively short time it classifies the event as a false alarm and
840 returns the RR estimation algorithm back to dry state operation. A similar approach, whereby a decision about the
841 presence or absence of rain is taken following an evaluation of the statistical behavior of the signal, is also pursued in
842 [8]. Also, following [8] it is worth remarking that signal variations induced by the satellite operator maneuvers can be
843 easily recognized if there are several GSs belonging to a regional network, all equipped with return links towards a
844 single data processing center. In such a case in fact signal variations occur simultaneously for all the terminals, and
845 therefore they can be identified and processed globally at a central level.

846 **6. Conclusions**

847 In this survey paper we have shown that in recent years - roughly in the last two decades - a considerable interest has
848 been devoted to novel low-cost techniques for early detection and evaluation of precipitations, relying on the oppor-
849 tunistic use of existing satellite networks, notably those based on geostationary satellites intended for domestic broad-
850 cast and internet access services. The underlying principle is conceptually simple although not necessarily easy to im-
851 plement, and it is based on the measurement of the attenuation introduced by the rain on the downlink signal, and on
852 the application of a proper inversion algorithm, appropriately geared to map this attenuation onto a rainfall rate esti-
853 mate. The above techniques have been studied with the aim to integrate or even replace the pre-existing infrastructures
854 based on rain gauges, radar sensors and meteorological satellites, with respect to which this new approach prospec-
855 tively offers greater pervasiveness and capillarity over the territory, thanks to the potentially huge number of terrestrial
856 terminals deployable in households, each amenable to act as a rain sensor. Another peculiar feature of these systems is
857 that of presenting an estimation accuracy independent of the site at which the terrestrial terminal is positioned, unlike
858 weather radars whose accuracy in providing estimates of instantaneous point-scale rain rate gets poorer and poorer as
859 the distance from the radar grows.
860 The material we have presented comes from the elaboration of a significant body of literature on the above topics. Since
861 the cited opportunistic approach has been proposed in support or as an alternative to traditional rain sensing tech-
862 niques, most papers delve into the relative performance of specific implementations of the new method with respect to
863 rain gauges and weather radars, notably with regard to their ability to measure the instantaneous rainfall rate and the
864 cumulated rainfall at a given geographical site. In this respect, one point of strength of the systems based on downlink
865 attenuation measurements is their sensitivity to the instantaneous rainfall rate, and this gives them an intrinsic aptitude
866 to operate in real-time alert networks, while rain gauges can only detect the cumulated rainfall in a certain time interval.
867 On the other hand, rain gauges yield measurements of the rain that has fallen at the exact geographical site where they
868 are deployed, while systems measuring the downlink signal attenuation are sensitive to the effect of the rain over the
869 entire "wet" section of the radio path between the satellite and the terrestrial receiver, and therefore are not strictly
870 suited for providing point-scale measurements. However this apparently poor compatibility of the new opportunistic
871 with respect to traditional sensors has been resolved by the various authors by resorting to a variety of *ad hoc* techniques
872 discussed in the paper.
873 The advantageous use of the opportunistic sensors requires that several collateral problems be addressed and solved.
874 In this paper we have identified, enumerated and discussed an exhaustive selection of these issues, and we have illus-
875 trated a number of solutions proposed in the literature, also highlighting their relative points of strength and weakness.
876 In summary, the issues to deal with for the implementation of a rain sensor based on measurements of satellite downlink

877 attenuation are substantially related to: *i*) identification of type of satellites and bands to be used, *ii*) identification of the
878 type of downlink signal, whether payload or beacon, on which to measure the rain-induced attenuation, also taking
879 into account the impact of this choice on the complexity and cost of the terrestrial receiver, *iii*) choice to be made between
880 the point-scale approach, in which each measurement of attenuation produced by a single terrestrial receiver is mapped
881 directly onto an estimate of the local rainfall rate, and the tomographic approach, in which the rainfall rate at each point
882 of the territory is estimated by processing several attenuation measurements collected from multiple radio links inter-
883 secting the rain field along different directions, *iv*) identification of an efficient algorithm for detecting the instants of
884 rain start and rain stop, *v*) identification of methods for estimating or monitoring the height of the rain volume and the
885 thickness of the melting layer, along with their respective specific attenuation coefficients, *vi*) identification of the time-
886 varying baseline against which to evaluate to rain-induced reduction of the relevant signal metric, either the SNR or the
887 ESNDR, and *vii*) evaluation of the algorithm latency and its compatibility with real-time operation.

888 With regard to the state of the art and future perspectives of the techniques covered in this paper, it is noted that most
889 of the algorithms proposed are still in the experimental phase, while only a few, such as those in [3], [8] and [6], [48]
890 have been brought to a more advanced level of validation and pre-engineering development.

891 In this respect, it cannot be ignored that a decisive factor for a widespread adoption of these techniques is the existence
892 on the market of commercial devices suited to facilitate their opportunistic usage. One instance is the SmartLNB, a
893 bidirectional device designed for domestic satellite TV which, as illustrated in Section 5.2.2, not only easily lends itself
894 to measuring the ESNDR on the downlink signal, but also allows measurement results and other processed data to be
895 transmitted back to a control station via a satellite return channel with no need for any additional terrestrial infrastruc-
896 ture. We observe that such a particular use of these devices could be currently considered at risk of decline due to the
897 rapid spread of internet TV platforms. On the other hand, the impetuous growth expected in the near future for satellite
898 IoT, prospectively guarantees many further years of bright future for interactive domestic satellite terminals.

899 Finally, we note that satellites could represent an excellent complementary technology to fill the coverage gaps of rain
900 monitoring networks based on the (far more mature) opportunistic use of terrestrial microwave links [11], as testified
901 by some very promising preliminary results presented in [71].

902

References

918 1. Barthès, F.; Mallet, C. Rainfall measurement from the opportunistic use of earth-space link in the Ku band. *Atmos. Meas. Tech.*
919   **2013**, *6*, 2181-2193, doi: 10.5194/amt-6-2181-2013.
920 2. Messer, H.; Sendik, O. A new approach to precipitation monitoring: a critical survey of existing technologies and challenges.
921   *IEEE Signal Process. Mag.* **2015**, *3*, 110–122, doi: 10.1109/MSP.2014.2309705.
922 3. Giannetti, F.; Reggiannini, R.; Moretti, M.; Adirosi, E.; Baldini, L.; Facheris, L.; Antonini, A.; Melani, S.; Bacci, G.; Petrolino, A.;
923   Vaccaro, A. Real-time rain rate evaluation via satellite downlink signal attenuation measurement. *MDPI Sensors*, **2017**, *17*, 1864,
924   doi: 10.3390/s17081864.
925 4. Arslan, C.H.; Aydin, K.; Urbina, J.V.; Dyrud, L. Satellite-link attenuation measurement technique for estimating rainfall accu-
926   mulation. *IEEE Trans. Geoscience and Remote Sens.* **2018**, *2*, 681-693, doi: 10.1109/TGRS.2017.2753045.
927 5. Gharanjik, A.; Bhavani Shankar, M.R.; Zimmer, F.; Ottersten, B. Centralized rainfall estimation using carrier to noise of satellite
928   communication links. *IEEE J. Sel. Areas Comm.* **2018**, *5*, 1065-1073, doi: 10.1109/JSAC.2018.2832798.
929 6. Colli, M.; Cassola, F.; Martina, F.; Trovatore, E.; Delucchi, A.; Maggiolo, S.; Caviglia, D.D. Rain fields monitoring based on
930   satellite microwave downlinks and traditional techniques in the city of Genoa. *IEEE Trans. Geosc. Rem. Sens.* **2020**, *9*, 6266-6280,
931   doi: 10.1109/TGRS.2020.2976137.

7. Adirosi, E.; Antonini, A.; Bacci, G.; Caparrini, F.; Facheris, L.; Giannetti, F.; Mazza, A.; Moretti, M.; Petrolino, A.; Reggiannini, R.; Vaccaro, A.; Baldini, L. NEFOCAST project for real-time precipitation estimation from Ku satellite links: preliminary results of the validation field campaign", *2nd URSI Atlantic Radio Science Conference*, Gran Canaria, **2018**, 1-4, doi: 10.23919/URSI-AT-RASC.2018.8471431.

8. Giannetti, F.; Moretti, M.; Reggiannini, R.; Vaccaro, A. The NEFOCAST system for detection and estimation of rainfall fields by the opportunistic use of broadcast satellite signals. *IEEE Aerospace and Electronic Systems Mag.* **2019**, 6, 16-27, doi: 10.1109/MAES.2019.2916292.

9. Christofilakis, V. *et al.* Earth-to-earth microwave rain attenuation measurements: a survey on the recent literature. *MDPI Symmetry.* **2020**, 12, 1440, doi: 0.3390/sym12091440.

10. Zheng, S. *et al.* Research on rainfall monitoring based on E-band millimeter wave link in East China. *MDPI Sensors.* **2021**, 21, 1670, doi: 10.3390/s21051670.

11. Cherkassky, D; Ostrometzky, J.; Messer, H. Precipitation classification using measurements from commercial microwave links. *IEEE Trans. Geosc. Rem. Sens.* **2014**, *52*, 2350-2356, doi: 10.1109/TGRS.2013.2259832.

12. Giuli, D.; Toccafondi, A.; Gentili G.B.; Freni A. Tomographic reconstruction of rainfall fields through microwave attenuation measurements. *J. Appl. Meteorol.* **1991**, *9*, 1323–1340, doi: 10.1175/1520-0450(1991)030<1323:TRORFT>2.0.CO;2.

13. Mishra, K.V.; Bhavani Shankar, M.R.; Ottersten, B. Deep rainrate estimation from highly attenuated downlink signals of ground-based communications satellite terminals. *IEEE Int. Conf. Acoust., Speech and Sign. Proc. (ICASSP).* **2020**, doi: 10.1109/ICASSP40776.2020.9054729.

14. Ramachandran, V.; Kumar, V. Rain attenuation measurement on Ku-band satellite TV downlink in small island countries. *Electronic Letters.* **2004**, 40, 8, 49-50, doi: 10.1049/el:20040019.

15. Freeman, R.L. *Radio system design for telecommunications*, 3rd ed.; IEEE-Wiley: New York, 2007.

16. D'Amico, M.; Manzoni, A.; Solazzi, G.L. Use of operational microwave link measurements for the tomographic reconstruction of 2-D maps of accumulated rainfall. *IEEE Trans. Geosc. Rem. Sens. Letters* **2016**, *12*, 1827-1831, doi: 10.1109/LGRS.2016.2614326.

17. Shen, X.;Huang, D.D.; Song, B.; Vincent, C.; Togneri, R. 3-D Tomographic reconstruction of rain field using microwave signals from LEO satellites: principle and simulation results. *IEEE Trans. Geosc. and Rem. Sens.* **2019**, *8*, 5434-5446, doi: 10.1109/TGRS.2019.2899391.

18. Cakaj, S. Rain attenuation impact on performance of satellite ground stations for low earth orbiting (LEO) satellites in Europe. *Int. J. Commun., Network and System Sc.* **2009**, *6*, 480-485, doi: 10.4236/ijcns.2009.26052.

19. "The European Table of Frquency Allocations and Application in the Frequency Range 8.3 kHz to 3000 GHz," ERC Report 25, ECC/CEPT, November 2020

20. ETSI TR 103 263 V1.2.1 (2016-02).

21. Recommendation ITU-R BO.1776-1 (01/2012), Maximum power flux-density for the broadcasting-satellite service in the band 21.4-22.0 GHz in Regions 1 and 3.

22. "Status of Telecommunication in W-band and possible applications: satellite broadband connection and networks of mobile phones," ARES & CTIF, University of Rome Tor Vergata, Rome, Italy, 26/09/ 2014. http://www.ares-consortium.org/It/wp-content/uploads/2016/03/2_Presentation_TOR.pdf [last visited: June 3, 2021]

23. Paulson, K.; Al-Mreri, A. A rain height model to predict fading due to wet snow on terrestrial links. *Radio Science* **2011**, *46*, RS4010. Doi:10.1029/2010RS004555.

24. Digital Video Broadcasting (DVB); Second generation framing structure, channel coding and modulation systems for Broadcasting, Interactive Services, News Gathering and other broadband satellite applications (DVB-S2), ETSI EN 302 307 V1.2.1 (2009-08).

25. Singh, M.S.J.; Hassan, S.I.S.; Ain, M.F.; Igarashi, K.; Tanaka K.; Iida, M. Analysis of tropospheric scintillation intensity on earth to space in Malaysia. *American J. of Appl. Sc.* **2006**, *3*, 2029-2032, doi: 10.3844/ajassp.2006.2029.2032.

26. Crane, R.K.; Blood, D.W. *Handbook for the estimation of microwave propagation effects – link calculation for earth-space paths*; Doc. no. P-7376-TR1, NASA Goddard Space Flight Center, June 1979.

27. Recommendation ITU-R P.840-5 (02/2012), Attenuation due to clouds and fog.

28. Recommendation ITU-R P.679-4, 2005: Propagation data required for the design of broadcasting-satellite systems.

29. Fortescue, P.W.; W. Stark, J.P. *Spacecraft Systems Engineering*; Wiley: Chichester, 2011.

30. Maral, G.; Bousquet, M. *Satellite Communication Systems*, 5th ed.; Wiley: 2002.

31. Borissov, S.; Wu, Y.; Mortari, D. East–West GEO satellite station-keeping with degraded thruster response. *Aerospace* **2015**, *2*, 581-601. https://doi.org/10.3390/aerospace2040581.

32. Matrosov, S.Y. Assessment of radar signal attenuation caused by the melting hydrometeor layer. *IEEE Trans. Geosc. and Rem. Sens.* **2008**, *4*, 1039-1047, doi: 10.1109/TGRS.2008.915757.

33. Matrosov, S.Y.; Clark, K.A.; Kingsmill, D.E. A polarimetric radar approach to identify rain, melting-layer, and snow regions for applying corrections to vertical profiles of reflectivity. *J. of applied meteorology and climatology* **2007**, *46.2*, 154-166, doi: 10.1175/JAM2508.1.

34. Dissanayake, A.W.; McEwan, N.J. Radar and attenuation properties of rain and bright band. *Proc. Int. Conf. Antennas and Propagation* **1978**, 125-129, Bibcode: 1978anpr.conf..125D.

35. Olsen, R.L.; Rogers, D.V.; Hodge, D.B. The aR^b relation in the calculation of rain attenuation. *IEEE Trans. Antennas Propag.* **1978**, 2, 318–329, doi: 10.1109/TAP.1978.1141845.

36. Recommendation ITU-R P.838-4, 2005: Specific attenuation model for rain for use in prediction methods.

37. Adirosi, E.; Baldini, L.; Roberto, N.; Vulpani, G.; Russo, F. Using disdrometer measured raindrop size distributions to establish weather radar algorithms. *AIP Conference Proceedings* **2015**, 1648, 190007, doi: 10.1063/1.4912476.

38. Adirosi, E.; Baldini, L.; Lombardo, F.; Russo, F.; Napolitano, F.; Volpi, E.; Tokay, A. Comparison of different fittings of drop spectra for rainfall retrievals. *Adv. Water Resour.* **2015**, *83*, 55–67, doi: 10.1016/j.advwatres.2015.05.009.

39. Arslan, C.H.; Aydin, K.; Urbina, J.; Dyrud, L.P.. Rainfall measurements using satellite downlink attenuation. *IEEE Geosc. Rem. Sens. Symp*. **2014**. doi: 10.1109/IGARSS.2014.6947391.

40. Xian, M.; Liu, X.; Gao, T. An improvement to precipitation inversion model using oblique earth-space link based on the melting layer attenuation. *IEEE Trans. Geosc. Rem. Sens.* **2020**. doi: 10.1109/TGRS.2020.3027465.

41. https://www.rec.ac.in/upload/SCS_M1_ECE-compressed.pdf [last visited: May 25, 2021]

42. "Essential characteristics for a Eutelsat W earthstation having the minimum required performance for Eurovision", EBU Tech 3288, April 1999.

43. https://www.satsig.net/eut2beac.htm [last visited: May 25, 2021]

44. http://frequencyplansatellites.altervista.org/Eutelsat/Eutelsat_10A.pdf [last visited: May 25, 2021]

45. http://frequencyplansatellites.altervista.org/Beacon-Telemetry_Europe-Africa-MiddleEast/Eutelsat_10A.html [last visited: May 25, 2021]

46. Amaya, C.; Nguyen, T. Propagation measurements in Ottawa with the Ka band beacon of the ANIK F2 satellite. *14th Int. Symp. Ant. Tech. and Applied Electromag. & American Electromag. Conf.* **2010**, pp. 1-4.

47. Kikkert, C.J.; Kenny, O.P. The design of a Ka band satellite beacon receiver . *IEEE 6th Int. Conf. on Inform., Comm. Sign. Proc.* **2007**, doi: 10.1109/ICICS.2007.4449689.

48. Colli, M.; Stagnaro, M.; Caridi, A.; Lanza, L.G.; Randazzo, A.; Pastorino, M.; Caviglia, D.D.; Delucchi, A. A field experiment of rainfall intensity estimation based on the analysis of satellite-to-earth microwave link attenuation. *Applications in Electronics Pervading Industry, Environment and Society*, Springer, **2019**, 137-144, doi: 10.1007/978-3-030-11973-7_1.

49. Colli, M.; Stagnaro, M.; Caridi, A.; Lanza, L.G.; Randazzo, A.; Pastorino, M.; Caviglia, D.D.; Delucchi, A. A field assessment of a rain estimation system based on satellite-to-earth microwave links. *IEEE Trans. Geosc. Rem. Sens.* **2019**, *5*, 2864-2875, doi: 10.1109/TGRS.2018.2878338.

50. Giro, R.A.; Luini L.; Riva, C.G. Rainfall estimation from tropospheric attenuation affecting satellite links. *MDPI Information* **2020**, *11*, doi: 10.3390/info11010011.

51. Bahri, R.; Keshavarzi, M.R.; Yarmohammadi, H.; Moradi, G. Typical Ka band satellite beacon receiver design for propagation experimentation. *7th Int. Symp. on Telecommunications (IST'2014)*, Sept. **2014**, doi: 10.1109/ISTEL.2014.7000686.

52. Recommendation ITU-R P.839-4, 2013: Rain height model for prediction methods.

53. Bryant, G.H.; Adimula, I.; Riva, C.; Brussard, G. Rain attenuation statistics from rain cell diameters and heights. *Int. J. Satellite Comm.* **2001**, 19:263-283 (DOI: 10.1002/sat.673).

54. Csurgai-Horváth, L.; Bító, J. Rain intensity estimation using satellite beacon signal measurements – A dual frequency study. *IEEE ISNCC 2018* **2018**, doi: 10.1109/ISNCC.2018.8530986.

55. Csurgai-Horváth, L. Small scale rain field sensing and tomographic reconstruction with passive geostationary satellite receivers. *MDPI Remote Sens.* **2020**, *12*, doi: 10.3390/rs12244161.

56. Mercier, F.; Barthès, F.; Mallet, C. Estimation of finescale rainfall fields using broadcast TV satellite links and a 4DVAR assimilation method. *J. of Atmos. and Oceanic Technol.* **2015**, *10*, 1709-1728, doi: 10.1175/JTECH-D-14-00125.1.

57. Arcidiacono, A.; Finocchiaro, D.; Collard, F.; Scalise, S.; Lazaro Blasco, F.; De Gaudenzi, R.; Cioni, S.; Alagha N.; Andrenacci, M. From S-MIM to F-SIM: Making Satellite Interactivity Affordable at Ku and Ka-band. *International Journal of Satellite Communications and Networking*. **2015**, January, 1-34, doi:10.1002/sat.1158.

58. Collard, F.; Recchia, A.; Antip, N.; Arcidiacono, A.; Finocchiaro, D.; Pulvirenti, O. Performance analysis of an enhanced spread spectrum Aloha system. In: Pillai P., Shorey R., Ferro E. (eds) Personal Satellite Services. *PSATS 2012*. Lecture Notes of the Institute for Computer Sciences, Social Informatics and Telecommunications Engineering **2012**, *52*, Springer, Berlin, Heidelberg.

59. Recommendation ITU-R PN.837-1 (08/1994), Characteristics of precipitation for propagation modelling.

60. Lolli, S. *et al*. Vertically resolved precipitation intensity retrieved through a synergy between the ground-based NASA MPLNET lidar network measurements, surface disdrometer datasets and an analytical model solution. *MDPI Remote Sensing* **2018**, *10*, doi: 10.3390/rs10071102.

61. Ojo, J.S. Rain height statistics based on 0°C isotherm height using TRMM precipitation data for earth-space satellite links in Nigeria. *ISRN Atmospheric Sciences* **2014**, article ID 798289, doi: 10.1155/2014/798289.

62. Mondal, N.C.; Sarkar, S.K. Rain height in relation to 0°C isotherm height for satellite communication over the Indian Subcontinent. *Theoretical and Applied Climatology* **2003**, doi: 10.1007/s00704-003-0002-y.

63. Mandeep, J.S. 0°C isotherm height for satellite communication in Malaysia. *Advances in Space Research* **2009**, 43.6, doi: 10.1016/j.asr.2008.09.013.

64. Badron, K. *et al*. Rain induced attenuation studies for V-band satellite communication in tropical region. *J. of Atmospheric and Solar-Terrestrial Physics* **2011**, *73.5*, doi: 10.1016/j.jastp.2010.12.006.

65. Sudarshana, K.P.S.; Samarasinghe, A.T.L.K.. Rain rate and rain attenuation estimation for Ku band satellite communications over Sri Lanka. *6th International Conference on Industrial and Information Systems*. **2011**, doi: 10.1109/ICIINFS.2011.6038030.

66. Emiliani, L.D.; Agudelo, J.; Gutierrez, E.; Restrepo,J.; Fradique-Mendez, C. Development of rain-attenuation and rain-rate maps for satellite system design in the Ku and Ka bands in Colombia. *IEEE Antennas and Propagation Magazine*. **2004**, 6, 54-68, doi: 10.1109/MAP.2004.1396736.

67. Tijani, A.; Yusuf, S.D.; Ibrahim, U.; Loko, A.Z., Mundi, A.A. Evaluation of real time rain-rate on downlink satellite signal attenuation in Abuja, Nigeria. *EDUCATUM Journal of Science, Mathematics and Technology*. 2020, 1, 29-38,doi: 10.37134/ejsmt.vol7.1.4.2020

68. Rieckner, M.R. *et al.* MERRA: NASA's modern-era retrospective analysis for research and applications. *J. of Climate*, **2011**, *7*, 3624-3648, doi: 10.1175/JCLI-D-11-00015.1.

69. Mugnai, C.; Sermi, F.; Cuccoli, F.; Facheris, L. Rainfall estimation with a commercial tool for satellite internet in Ka band: model evolution and results. *2015 IEEE Geosc. Rem. Sens. Symp.* **2015**, 890-893, doi: 10.1109/IGARSS.2015.7325908.

70. Baldini, L.; Gorgucci, E. Identification of the melting layer through dual-polarization radar measurements at vertical incidence. *J. of Atmos. and Oceanic Technol.* **2006**, *6*, 829-839, doi: 10.1175/JTECH1884.1.

71. Saggese, F.; Giannetti, F.; Lottici, V, A novel approach to rainfall rate estimation based on fusing measurements from terrestrial microwave and satellite links. *XXXIII General Assembly and Scientific Symposium of the International Union of Radio Science*, **2020**, 1-4, doi: 10.23919/URSIGASS49373.2020.9232257.